

# **Impact Modeling and Dynamic Failure of Ballistic Steel Structures**

by

Luyue Mao

A thesis submitted in partial fulfillment of the requirements for the degree of

Master of Science

Department of Mechanical Engineering  
University of Alberta

© Luyue Mao, 2024

# Abstract

In this thesis, an advanced stress-state- and strain-rate-dependent model, Generalized Incremental Stress State dependent damage MOdel (GISSMO), is implemented to predict the ballistic responses of Armox 500T steel under high-velocity impact in finite element solver LS-DYNA/Explicit. The GISSMO is calibrated using tensile simulations against the force-displacement data and validated using the comparisons between quantitative (e.g., projectile residual velocity and hole size after impact) and qualitative experimental measurements (e.g., fracture behaviors with plate spalling and bulging) from the literature. Then, the GISSMO is used to model ballistic responses of a bi-layer Armox 500T steel system. Here, ballistic simulations are conducted to explore the roles of the standoff distance and impact angle of obliquity on impact failure behaviors of bi-layered steel systems. Results indicate that a large increase of the projectile yaw and deflection is observed and measured from plates with no standoff distance and a 20 mm standoff distance under a 30 deg oblique impact from a fragment simulating projectile (FSP) compared with the normal impact. In addition, the standoff distance has a larger influence on projectile residual velocity when the FSP impacts the plate at an oblique angle of 30 deg. Overall, the work from this study demonstrates a better ballistic prediction for Armox 500T steel using the GISSMO and provides novel insights into lightweight and high-performing armor structures.

# Preface

This thesis titled, “Impact Modelling and Dynamic Failure of Ballistic Steel Structures” is originally from the work done by Luyue Mao.

- The Chapter 2 of this thesis has been published in the *International Journal of Impact Engineering* as **Kyle Mao**, Geneviève Toussaint, Alexandra Komrakova, and James D. Hogan, “High-Velocity Impact Failure Modeling of Ar-mox 500T Steel: Model Validation and Application to Structural Design”. Kyle Mao responded to conceptualization, simulations and the manuscript composition. Geneviève Toussaint contributed to conceptualization and manuscript edits. Alexandra Komrakova was the co-supervisory author and contributed to manuscript edits. James D. Hogan was the supervisory author and contributed to the conceptualization and manuscript composition.

*“No matter how hard you work, someone else is working harder.”*

*- Elon Musk*

# Acknowledgments

Foremost, I wish to express my deepest gratitude and appreciation to my supervisor for my entire graduate study, Dr. James D. Hogan. His professional deliveries, guidance and mentorship, patience and encouragement deeply influence me and help in my professional development throughout my master's study journey. I would also like to thank him for providing inspired feedback, academic resources, and opportunities for leadership and collaboration, which have made me a professional scientific researcher. I would also like to deliver my sincere appreciation to my co-supervisor, Dr. Alexandra Komrakova, for providing insightful ideas and guidance, countless feedback, and most important continuous encouragement.

I wish to acknowledge my great appreciation to the Centre for Design of Advanced Material (CDAM) research lab colleagues. First, I would like to thank the project manager Cass (Haoyang) Li and postdoctoral fellow Kasra Rezasefat Balasbaneh, for their great knowledge deliveries, guidance and collaboration. I appreciate the novel discussions and guidance from Saman Sayahlatifi, Sara Sheikhi, Yogesh Kumar. Then, Harshil Hitesh Pisavadia, thanks for his time to discuss science, encouragement and collaboration. Last but not least, I would also like to thank academic collaborators and industrial partners in the project. I sincerely appreciate Geneviève Toussaint and Harry Templeman for mentoring, time for caring, and scientific discussion.

I wish to express my great appreciation to my parents, Zhanjun Mao and Lifeng Jiao, for their unconditional love, continual support, and endless belief in my life and study journey. I am extremely grateful to the whole family and also my grandparents, Rugui Mao and Yu e Liu, Jiazhen Jiao and Bingwei Li, for their trust, encouragement,

dedication and support. A special appreciation to my girlfriend, Chuannan Luo, for her beliefs and love.

Finally, I would like to say, "Don't let the defeat dishearten you! Remember that Rome was not built in a day". I will keep working hard and make life shine and be meaningful!

This work is supported by Defence Research and Development Canada (DRDC), General Dynamics Land Systems-Canada, and NP Aerospace through NSERC Alliance project ALLRP 560447-2020. The views and conclusions contained in this document are those of the authors and should not be interpreted as representing the official policies, either expressed or implied, of General Dynamics, NP Aerospace, DRDC or the Government of Canada. The Government of Canada is authorized to reproduce and distribute reprints for Government purposes notwithstanding any copyright notation herein. This research was also enabled in part by support provided by Compute Ontario ([www.computeontario.ca/](http://www.computeontario.ca/)) and Compute Canada ([www.computecanada.ca](http://www.computecanada.ca)) via the Graham cluster. In addition, this research work was also funded by the Department of National Defence (DND) of Canada program Innovation for Defence Excellence and Security (IDEaS) under Project W7714-228051/001/SV1.herein.

# Table of Contents

<b>1</b>	<b>Introduction</b>	<b>1</b>
1.1	Motivation . . . . .	1
1.2	Thesis Objectives . . . . .	2
1.3	Thesis Goals . . . . .	3
1.4	Thesis Contributions . . . . .	4
1.5	Thesis Structure . . . . .	4
<b>2</b>	<b>High-Velocity Impact Failure Modeling of Armox 500T Steel: Model Validation and Application to Structural Design</b>	<b>6</b>
2.1	Introduction . . . . .	7
2.2	Methodology . . . . .	11
2.2.1	Generalized Incremental Stress State Dependent Damage Model (GISSMO) . . . . .	11
2.2.2	Rationale of the GISSMO Implementation . . . . .	13
2.3	Numerical Simulations with the GISSMO Implementation . . . . .	15
2.3.1	Parameter Determination and Calibration for the GISSMO . . . . .	15
2.3.2	GISSMO Validation . . . . .	22
2.3.3	Numerical Setups of the Structural Design Application . . . . .	27
2.4	Results and Discussion . . . . .	31
2.4.1	Impact Failure Behaviors of Bi-Layered Steel Systems . . . . .	31
2.4.2	Impact Failure Behaviour of the Projectile . . . . .	37

2.4.3	The Role of Standoff Distance and Angle of Obliquity on Ballistic Responses of the Bi-Layered Steel Systems . . . . .	38
2.5	Conclusions . . . . .	41
<b>3</b>	<b>Conclusion and Future Works</b>	<b>43</b>
3.1	Implications . . . . .	43
3.2	Future Work and Recommendations . . . . .	44
	<b>Bibliography</b>	<b>47</b>
<b>4</b>	<b>Appendix</b>	<b>57</b>
4.1	Constitutive Model Description . . . . .	57
4.1.1	Johnson-Cook Material Model . . . . .	57
4.1.2	Equations of State . . . . .	58
4.2	Mesh Sensitivity Analysis . . . . .	61

# List of Tables

2.1	Comparison of projectile residual velocity and perforation hole diameter between experimental ballistic results from Iqbal et al. (2016) [2] and LS-DYNA simulation results. . . . .	26
2.2	Impact configurations to investigate the role of the standoff distance and angle of obliquity on the ballistic performance of the steel armor system. The maximum depth of penetration for a 12.7 mm thick RHA plate, minimum RHA plate thickness required to stop the projectile, and mass of the bi-layer plates are compared for the different noted impact configurations. . . . .	29
4.1	Material model properties and constants of the 12.7 mm armor piercing incendiary projectile. . . . .	59
4.2	Material model properties and constants of the rolled homogeneous armor steel and the 4340 steel. . . . .	60

# List of Figures

2.1	The flow chart for the GISSMO implementation. . . . .	14
2.2	Parameterization of the GISSMO input surfaces: (a) fracture surface of the ArmoX 500T steel and (b) instability surface of the ArmoX 500T steel. The surfaces are produced using the biharmonic spline interpolation function in MATLAB based on the experimental data from Popławski et al. (2020) [4]. . . . .	17
2.3	Equivalent plastic strain at fracture data from Iqbal et al. (2016) [2] used to account for strain rate effect into the established GISSMO. . . . .	18
2.4	Tensile model configuration in LS-DYNA with symmetric boundary conditions used for the GISSMO calibration. Geometry and dimensions of the model are from Popławski et al. (2020) [4]. . . . .	19
2.5	Force-displacement curve of numerical results for different element sizes plotted against experimental results from Popławski et al. (2020) [4]: (a) before applying the mesh regularization function, (b) fade and mesh regularization curve used in the GISSMO calibration, (c) after applying the mesh regularization function, and (d) comparison of numerical results for an alternative boundary condition with a smaller clamping area. . . . .	21
2.6	Numerical setups for ballistic impact of a 10 mm thick ArmoX 500T steel plate subjected to impact by the 12.7 mm armor piercing incendiary projectile. Geometries with dimensions are replicated from Iqbal et al. (2016) [2]. . . . .	24

2.7	Comparison of projectile residual velocity in LS-DYNA simulation and numerical results from Iqbal et al. (2016) [2] and calculated results from the Recht–Ipson model [85]. . . . .	26
2.8	Ballistic simulation configuration consisting of a 10 mm thick Armox 500T steel front plate and 12.7 mm thick RHA back plate with no standoff distance under a normal impact from a 20 mm fragment simulating projectile. Geometries of the FSP are replicated from MIL-DTL-46593B (MR) [92]. . . . .	30
2.9	Projectile kinetic energy plotted against time with corresponding impact failure behaviors at noted time instances for a configuration of a 10 mm thick Armox 500T steel front plate and 12.7 mm thick RHA back plate impacted by a FSP at 1000 m/s: (a1) plates with no standoff distance under a normal impact and (a2) plates with a 20 mm standoff distance under a normal impact, and (b1) plates with no standoff distance under a 30 deg oblique impact and (b2) plates with a 20 mm standoff distance under a 30 deg oblique impact. . . . .	33
2.10	Impact failure behaviors at noted time instances for different configurations for a 1000 m/s impact from a fragment simulating projectile: (a) Configuration 1, (b) Configuration 2, (c) Configuration 3, and (d) Configuration 4. Configurations 1 and 2 shows plug formation as the dominant impact failure mechanism. Larger size of plugs are formed and observed in Configuration 1 than Configuration 2 as the projectile penetrates. The basic impact failure behaviors of the plates impacted by the FSP can be identified as frontal spallation, shear dominated fracture, delamination of layers, and bulging of the plates. Moreover, the failure behaviors of Configurations 3 and 4 involves petaling and plugging. It is observed that larger plugs results in larger petals and larger structural deformations of the RHA plate in Configuration 3. . . . .	36

2.11	Projectile yaw angle plotted against projectile displacement and projectile residual velocity plotted against time with corresponding insets of the deformed projectiles at noted time instances for a 1000 m/s impact from a fragment simulating projectile: (a) Configuration 1, (b) Configuration 2, (c) Configuration 3, and (d) Configuration 4. The four configurations consist of the 10 mm thick Armox 500T steel front plate and the RHA back plate with the minimum thickness required to stop the projectile ( $v = 0$ m/s and thicknesses for a given configuration noted in Table 2.2). A large yaw angle is measured for Configurations 3 and 4, and this indicates the angle of obliquity could lead to greater resulting time-evolved yaw angles. Comparing Configurations 1 and 2, and 3 and 4, the angle of obliquity has more effects on the changes of the deflection angle of the projectile than the standoff distance. . . .	39
2.12	Projectile residual velocity plotted against time for a 10 mm thick Armox 500T steel front plate and a 3 mm thick RHA back plate with corresponding failure modes at noted time instances for a 1000 m/s impact from a fragment simulating projectile: (a) plates with no standoff distance under a normal impact, (b) plates with a 20 mm standoff distance under a normal impact, (c) plates with no standoff distance under a 30 deg oblique impact, and (d) plates with a 20 mm standoff distance under a 30 deg oblique impact. It is observed that final projectile residual velocities of Configurations 2 and 4 are greater than Configurations 1 and 3, respectively, and this indicates the in-contact plate system has a better ballistic resistance than the plates with a standoff distance. . . . .	40

4.1 A mesh sensitivity study (i.e., mesh size 0.2 mm, 0.35 mm, and 0.5 mm) using the GISSMO in the simulations consisting of a 10 mm thick Armox 500T steel front plate and 4.70 mm thick rolled homogeneous armor back plate with no standoff distance under a normal impact from a 20 mm fragment simulating projectile. The simulated hole size of the Armox 500T steel plate and formulated plug made by the projectile are compared at different mesh sizes. . . . . 62

# List of Symbols

## Greek

$\bar{\sigma}$	Flow stress, Johnson-Cook model
$\dot{\epsilon}_0$	Equivalent plastic strain rate, Johnson-Cook model
$\dot{\epsilon}$	Reference strain rate, Johnson-Cook model
$\rho$	Density, Johnson-Cook model
$\epsilon^{pl}$	Equivalent plastic strain, Johnson-Cook model
$A$	Static yield stress, Johnson-Cook model
$B$	Strain hardening constant, Johnson-Cook model
$C$	Strain rate constant, Johnson-Cook model
$c_p$	Specific heat, Johnson-Cook model
$D_1$	Damage constant, Johnson-Cook model
$D_2$	Damage constant, Johnson-Cook model
$D_3$	Damage constant, Johnson-Cook model
$D_4$	Damage constant, Johnson-Cook model
$D_5$	Damage constant, Johnson-Cook model
$E$	Young's modulus, Johnson-Cook model
$G$	Shear modulus, Johnson-Cook model
$m$	Thermal softening coefficient, Johnson-Cook model

$n$	Strain hardening coefficient, Johnson-Cook model
$T_c$	Current temperature of material, Johnson-Cook model
$T_m$	Melting temperature of material, Johnson-Cook model
$T_{room}$	Room temperature of material, Johnson-Cook model
$\nu$	Poisson's Ratio, Johnson-Cook model
$\gamma_0$	Grüneisen gamma coefficient, Mie-Grüneisen equations of state
$\mu$	Volumetric strain defining current density to reference density, Mie-Grüneisen equations of state
$\rho_0$	Density at the reference state, Mie-Grüneisen equations of state
$a$	Volume correction factor, Mie-Grüneisen equations of state
$C'$	Bulk speed of sound, Mie-Grüneisen equations of state
$E'$	Internal energy per unit reference specific volume, Mie-Grüneisen equations of state
$P$	Hydro-static pressure, Mie-Grüneisen equations of state
$S_i$	Slope coefficients of the shock and particle velocity curve ( $i=1,2,3$ ), Mie-Grüneisen equations of state
$\bar{\theta}$	Lode angle parameter, Generalized Incremental Stress State Dependent Damage MOdel
$\Delta D$	Incremental damage factor, Generalized Incremental Stress State Dependent Damage MOdel
$\Delta F$	Incremental instability factor, Generalized Incremental Stress State Dependent Damage MOdel

$\eta$	Stress triaxiality, Generalized Incremental Stress State Dependent Damage Model
$\sigma_c$	Current stress, Generalized Incremental Stress State Dependent Damage Model
$\sigma_i$	Principal stress ( $i=1,2,3$ ), Generalized Incremental Stress State Dependent Damage Model
$\sigma_m$	Hydro-static stress, Generalized Incremental Stress State Dependent Damage Model
$\sigma_m^*$	Modified stress coupled to damage, Generalized Incremental Stress State Dependent Damage Model
$\sigma_{vm}$	Von Mises stress, Generalized Incremental Stress State Dependent Damage Model
$\theta$	Lode angle, Generalized Incremental Stress State Dependent Damage Model
$\varepsilon^{pl}$	Current equivalent plastic strain, Generalized Incremental Stress State Dependent Damage Model
$\varepsilon_{crit}$	Equivalent plastic strain at the onset of necking, Generalized Incremental Stress State Dependent Damage Model
$\varepsilon_f$	Equivalent plastic strain at fracture, Generalized Incremental Stress State Dependent Damage Model
$D$	Damage factor, Generalized Incremental Stress State Dependent Damage Model
$D_{crit}$	Critical threshold damage, Generalized Incremental Stress State Dependent Damage Model
$F$	Instability factor, Generalized Incremental Stress State Dependent Damage Model
$m$	Fade exponent, Generalized Incremental Stress State Dependent Damage Model

- $n$  Damage exponent, Generalized Incremental Stress State Dependent Damage Model
- $p$  Hydrostatic pressure, Generalized Incremental Stress State Dependent Damage Model
- $s$  Deviatoric stress tensor, Generalized Incremental Stress State Dependent Damage Model
- $D^*$  Updated damage, Generalized Incremental Stress State Dependent Damage Model

# Abbreviations & Acronyms

**2D** Two-dimensional.

**3D** Three-dimensional.

**EOS** Equation of state.

**FEM** Finite element method.

**FSP** Fragment simulating projectile.

**GISSMO** Generalized Incremental Stress State dependent damage MOdel.

**GTN** Gurson Tvergaard Needleman.

**JC** Johnson-Cook.

**RHA** Rolled homogeneous armour.

# Chapter 1

## Introduction

### 1.1 Motivation

Armox 500T steel is increasingly being used in personal protective equipment and hybrid armor systems within armored vehicle structures due to its high hardness, fracture strength, and impact toughness [1–4]. In the literature, the fracture behavior of Armox 500T steel has been experimentally investigated. For instance, Iqbal et al. [2] experimentally studied the stress-strain relations of Armox 500T steel by using different notched radii of cylindrical samples. They also investigated ballistic resistance for both 8 mm and 10 mm thick plates made of Armox 500T steel under high-velocity impact. There are only limited experimental data sets (e.g., velocity and plate thickness ranges [2]) in the literature because of the high cost of materials and limitations in diagnostic methods for extracting impact-related properties and phenomena (e.g., ballistic spalling). In addition, the numerical studies are conducted to explore the responses of Armox 500T steel (e.g., ballistic limit [2], residual stress [5, 6], and energy dissipation [7]), including the effect of structural geometries (e.g., thickness [2], areal density [8]) under various ballistic impact conditions. For instance, Iqbal et al. [2] determined the model parameters of the Johnson-Cook model for Armox 500T steel based on their experimental data, and predicted the ballistic limits for both 8 mm and 10 mm thick Armox 500T steel. Specifically, The Johnson-Cook model, as a phenomenological model, incorporates the effect of stress triaxiality on

fracture prediction, but the effect of the Lode angle is not included in the framework of the Johnson-Cook model [9]. The Lode angle parameter has been identified as an important parameter in the ductility description, damage evolution, and fracture prediction of materials to capture the relationship between the three principal stresses and the intermediate stress [10–13]. These considerations have been shown to be important in Armox 500T steel [4]. As a suitable alternative, the Generalized Incremental Stress State dependent damage MOdel (GISSMO) accounts for the stress triaxiality and Lode angle dependence to predict the onset of fracture [14–16]. Therefore, building on limitations on experimental work and modeling approach, this study provides an improved constitutive model to describe the ballistic performance of Armox 500T steel towards informing the design impact protection systems using finite element simulations in LS-DYNA R11.1 software.

## 1.2 Thesis Objectives

The objective of this thesis is to simulate the dynamic and impact failure behavior of Armox 500T steel under the high-velocity ballistic impact using the Generalized Incremental Stress State dependent damage MOdel (GISSMO) in LS-DYNA R11.1 software. The parameter determination, calibration, and validation of the stress state- and strain rate-dependent GISSMO are well-introduced for Armox 500T steel in this thesis. The importance of this thesis is identified: (1) this study provides clear descriptions of GISSMO implementation for Armox 500T steel used for high-velocity ballistic impact cases, (2) it provides novel insights into armor structural designs made by Armox 500T steel, and (3) Simulating bi-layered Armox 500T steel-based systems explores impact failure behaviors, the role of standoff distance, and angle of obliquity of the projectile.

## 1.3 Thesis Goals

To accomplish the thesis objective, the following goals will be pursued:

1. Parameterizing the fracture-related properties of Armox 500T steel by developing the fracture surface (i.e., equivalent plastic strain at fracture as a function of the stress triaxiality and Lode angle parameter) and instability surface (i.e., equivalent plastic strain at the onset of necking as a function of the stress triaxiality and Lode angle parameter) for Armox 500T steel using data from the literature [4].
2. Calibrating the GISSMO (i.e., determining the fade exponent and mesh regularization curves) by simulating a thin double-grooved specimen under uniaxial tension in LS-DYNA software and comparing simulated force-displacement results with the experimental data from the literature [4].
3. Validating the GISSMO by simulating ballistic impact models against experimental data [2] (e.g., projectile residual velocity, hole size of Armox 500T steel plate made by the projectile, impact failure behaviors such as the frontal spallation).
4. Simulating ballistic responses of bi-layered Armox 500T steel-based armor systems using the validated GISSMO to explore: (1) impact failure behaviors, (2) the role of standoff distance, (3) angle of obliquity of the projectile.

## 1.4 Thesis Contributions

The contributions from this thesis are summarized below:

1. Made novel contributions in simulating the ballistic impact of Armox 500T steel using an advanced fracture model (i.e., GISSMO). The rationale for the GISSMO implementation for Armox 500T steel is well-introduced in this thesis and to date, no studies have developed a GISSMO for Armox 500T steel.
2. Simulated bi-layered Armox 500T steel-based systems to identify the impact failure behaviors, the role of standoff distance, and the impact angle of obliquity of the projectile. Results provide new capabilities to the design of lightweight and high-performing steel-based armor structures.

## 1.5 Thesis Structure

The thesis structure is presented as follows:

1. Chapter 1 outlines the motivation, objectives, goals, contributions, and structure of this thesis.
2. Chapter 2 introduces the GISSMO implementation for Armox 500T steel, including parameterizing the fracture-related properties of Armox 500T steel, determining the numerical settings (e.g., fade exponent and mesh regularization functions) using quasi-static tensile simulations, and validating the GISSMO using ballistic impact simulations. In addition, the role of standoff distance and angle of obliquity of the projectile on impact failure behaviors of bi-layered Armox 500T steel-based armor systems are explored. This part of the thesis has been published in the *International Journal of Impact Engineering* with “High-Velocity Impact Failure Modeling of Armox 500T Steel: Model Validation and Application to Structural Design”.

3. Chapter 3 describes the key outcomes, limitations, and future work of the thesis study, focusing on the validity and feasibility demonstration of impact failure modeling using the GISSMO, the current limitation of the thesis study, and future recommendations on improving fracture prediction of the GISSMO in terms of material stress state characterization, and addressing strain rate- and temperature-effect into the GISSMO.

## Chapter 2

# High-Velocity Impact Failure Modeling of Armox 500T Steel: Model Validation and Application to Structural Design

Part of this Chapter was published as **Kyle Mao**; Geneviève Toussaint; Alexandra Komrakova; and James D. Hogan. *High-Velocity Impact Failure Modeling of Armox 500T Steel: Model Validation and Application to Structural Design*. International Journal of Impact Engineering., vol. 183, no. 104790, p. 104790, 2024.

---

Author	Contributions
Kyle Mao	Conceptualization, Methodology, Software, Calibration, Validation, Visualization, Numerical analysis, Writing - original draft
Geneviève Toussaint	Conceptualization, Validation, Writing – review & editing
Alexandra Komrakova	Writing – review & editing, Supervision
James D. Hogan	Principal investigator, Conceptualization, Writing – review & editing, Supervision

---

## 2.1 Introduction

Armox 500T steel is increasingly used in personal protective equipment and hybrid armor systems within armored vehicle structures due to its high hardness, fracture strength, and impact toughness [1–4]. In the literature, this ballistic of the material has been investigated experimental and numerically (e.g., ballistic limit [2], residual stress [5, 6], and energy dissipation [7]), including the effect of structural geometries (e.g., thickness [2], areal density [8]) under various ballistic impact conditions. For instance, Iqbal et al. [2] experimentally studied the ballistic resistance and predicted ballistic limits for both 8 mm and 10 mm thick plates made of Armox 500T steel under high-velocity impact. There are only limited experimental data sets (e.g., velocity and plate thickness ranges [2]) in the literature because of the high cost of materials and limitations in diagnostic methods for extracting impact-related properties and phenomena (e.g., change of mechanisms). Therefore, numerical approaches are often employed to study ballistic responses of the materials in multi-layered configurations [17, 18]. This study provides an improved constitutive model to describe the ballistic performance of Armox 500T steel and could be used to design armor systems more efficiently using finite element simulations.

The ballistic performance of armor systems is influenced by different factors, including properties of the material [19–21], impactor type and impact velocity [22, 23], impact angle of obliquity, number, order, and thickness of layers [24–26]. Past efforts have been focused on exploring the effectiveness among the monolithic, in-contact, and multi-layered plate configurations [27–31], and the standoff distance in multi-layered plates [32–37]. Corran et al. [27] carried out impact experiments on various target combinations against different projectiles (e.g., nose shape and mass) and found that the in-contact plates had better performance compared to the equivalent monolithic plates subjected to impact from a blunt projectile impact. In addition, according to the perforation energy results from their study, the in-contact plates of-

ferred better ballistic resistance than plates with a 12 mm standoff distance. In another study, Zhang et al. [35] experimentally studied the ballistic responses of multi-layered metallic targets against blunt projectiles, and they concluded that targets with a bigger standoff distance (i.e., 100 mm) had better ballistic resistance than targets with a smaller standoff distance (i.e., 6 mm). Here, this study aims at developing a better understanding of the roles of the standoff distance (i.e., 0 and 20 mm) and angle of obliquity (i.e., 0 and 30 deg) on the impact failure behaviors of Armox 500T steel while considering a lightweight design. A bi-layer armor system is constructed with an Armox 500T steel front plate backed by a rolled homogeneous armor (RHA) steel plate that is impacted by a 20 mm fragment simulating projectile (FSP). To better predict the ballistic performance of the system, an appropriate modeling which is capable of describing the material plasticity and fracture-mechanical behavior is required.

In the literature, multiple modeling approaches have been employed to investigate the mechanical responses of ductile materials under dynamic impact. For example, micromechanical-based models, such as the Gurson Tvergaard–Needleman (GTN) model [38], have been used for predicting crack initiation and propagation via void nucleation and growth [39, 40]. Alternatively, phenomenological constitutive models, such as the Johnson-Cook (JC) model [41, 42], Zerilli-Armstrong model [43], and Lemaitre model [44], have also been used to describe the fracture behaviors of ductile materials (e.g., Johnson-Cook model for Armox 500T steel [2, 8, 45–50]). However, the JC damage model incorporates the effect of stress triaxiality without accounting for the effect of Lode angle parameter, which has been shown to be important by Popławski et al. [4]. In addition, other studies have also identified that Lode angle parameter plays an important role in the ductility description, damage evolution, and fracture prediction of materials [10–13] because it captures the relationship between the three principal stresses and the intermediate stress. For example, the importance on Lode-dependent plasticity behaviors and accuracy on ballistic responses of

ZK61m magnesium alloy were demonstrated in the study done by Deng et al. [12]. They found that the fracture loci of the material is significantly sensitive to Lode angle and demonstrated that introducing the Lode angle parameter to the plasticity and fracture models can improve the accuracy of the ballistic prediction. In a recent study, Popławski et al. [4] found that the fracture properties of Armox 500T steel were dependent on stress triaxiality and the Lode angle parameter. As an alternative to the JC model, the Generalized Incremental Stress State dependent damage MOdel (GISSMO) was proposed to predict the onset of fracture [14, 15] incorporating the stress triaxiality and Lode angle parameter [16]. In the GISSMO framework incorporating the effects of stress triaxiality and Lode angle parameter, the damage is non-linearly accumulated under non-proportional strain paths until fracture; this is important because the stress triaxiality is not constant during the deformation of the material and equivalent plastic strain at fracture does not remain the same at different stress triaxiality [51]. The accumulated instability intensity defines the necking occurrence and initiates the coupling procedure of the damage and stress tensor until the fracture [51]. To date, no studies have developed a GISSMO for Armox 500T steel, thus motivating our current efforts.

Past studies have implemented GISSMO for modeling crashworthiness [52–54], sheet metal forming processes [55], self-pierce riveting process [56, 57], 3D-printed structures applications [58, 59], and blast loading [9, 60]. Dai et al. [54] developed the GISSMO associated with fully characterized stress state for quenched boron steel. In their study [54], the effectiveness of the GISSMO in fracture modeling of the crashworthiness analysis has been demonstrated through both simulated and experimental results on quantitative (i.e., force-displacement curves) and qualitative (i.e., deformation mode) measures. In another study, Polyzois and Toussaint [9] studied the fracture properties of the AlgoTuf 400F steel and accurately reproduced blast experiments in terms of fractography and target deformation using the GISSMO in LS-DYNA software. These studies [61–66] have shown that the GISSMO enables

better fracture prediction in modeling impact events. Altogether, the GISSMO has been chosen in this study as the model framework to predict ductile fracture of Armox 500T steel: (1) its path-dependent fracture and instability criterion captures the stress state-dependent material fracture behavior, resulting in more accurate reproduction of experiments involving Armox 500T (e.g., tensile testing [51, 67] and ballistic impact [64, 68]), (2) its fade exponent function controls a given state of stress fading and this is important because it governs the rate of energy dissipation [15] (3) its regularization feature can reduce the mesh size sensitivity on fracture prediction, where larger element sizes can be used to reduce the computational time and scale the fracture surface of the material to a range of different element sizes [69], and (4) its fracture parameters can be scaled associated with the strain rate to describe the material behavior under high strain rate conditions [2].

This study built on previous efforts on failure modeling of Armox 500T steel [2, 4] to implement the strain rate- and stress state-dependent GISSMO in ballistic impact events. The framework of this paper is as follows: firstly, the computational models used in LS-DYNA simulations are described (see Section 2.2). Secondly, model parameters of the Armox 500T steel consisting of the fracture and instability surface data are extracted from the literature [4], and implemented into the GISSMO in LS-DYNA finite element code (see Section 2.3.1). Thirdly, strain rate dependent equivalent plastic strain at fracture data of Iqbal et al. [2] are used and integrated into the GISSMO, and a quasi-static tensile simulation is then performed to determine the fade exponent and mesh regularization functions in the GISSMO (see Section 2.3.1). Next, ballistic impact experiments presented in [2] are reproduced (see Section 2.3.2). Finally, the validated model is used to study structural design of bi-layered Armox 500T armor with considerations for minimizing the back plate thickness and system weight (see Section 2.3.3 and 2.4).

## 2.2 Methodology

In this study, the LS-DYNA/Explicit R11.1 software is chosen for computational finite element modeling because it is well-suited for simulating structural-scale ballistic impact cases [70]. The phenomenological Generalized Incremental Stress State dependent damage MOdel (GISSMO), which has been integrated into the LS-DYNA finite element code, is used to describe the fracture behavior of Armox 500T steel and to predict impact failure undergoing strain rate- and stress state-dependent loading [2, 4]. The present study focuses on the GISSMO parameterization for the Armox 500T steel and its validation with ballistic simulations. In the following sections, parameters determination and calibration are shown (see Section 2.3.1), and model validation is demonstrated (see Section 2.3.2).

### 2.2.1 Generalized Incremental Stress State Dependent Damage MOdel (GISSMO)

The stress triaxiality dependent GISSMO was proposed by Neukamm et al. [14, 15], and the Lode angle dependence was studied by Basaran et al. [16]. The GISSMO describes ductile damage evolution and predicts the fracture initiation incorporating incremental damage and instability formulations. The GISSMO algorithm defines an evolution law of the phenomenological damage factor ( $D$ ) in an exponential equivalent plastic strain formulation shown in Equation (2.1).

$$D = \left( \frac{\varepsilon^{pl}}{\varepsilon_f(\eta, \bar{\theta})} \right)^n \quad (2.1)$$

where  $n$  is the damage exponent that defines the non-linearity of damage evolution,  $\varepsilon^{pl}$  is the current equivalent plastic strain, and  $\varepsilon_f(\eta, \bar{\theta})$  is the equivalent plastic strain at fracture as a function of stress triaxiality ( $\eta$ ), and Lode angle parameter ( $\bar{\theta}$ ). When  $D = 0$ , the material is intact, and when  $D = 1$ , failure occurs. The stress triaxiality ( $\eta$ ) defines the ratio of the hydrostatic stress ( $\sigma_m$ ) or hydrostatic pressure ( $p$ ) to the von Mises stress ( $\sigma_{vm}$ ) [71], and the Lode angle parameter ( $\bar{\theta}$ ) is defined as the third

deviatoric stress invariant to quantify the stress deviation state [72], as defined in Equation (2.2) and (2.3), respectively:

$$\eta = \frac{\sigma_m}{\sigma_{vm}} = -\frac{p}{\sigma_{vm}} \quad (2.2)$$

$$\bar{\theta} = \cos(3\theta) = \frac{27 \det(s)}{2 \sigma_{vm}^3} \quad (2.3)$$

where  $\sigma_m = \frac{\sigma_1 + \sigma_2 + \sigma_3}{3}$ ,  $\sigma_{vm} = \sqrt{\frac{(\sigma_1 - \sigma_2)^2 + (\sigma_2 - \sigma_3)^2 + (\sigma_3 - \sigma_1)^2}{2}}$  with  $\sigma_1, \sigma_2, \sigma_3$  being three principal stresses,  $s$  is the deviatoric stress tensor, and  $\theta$  is the Lode angle.

In the GISSMO algorithm, the damage factor ( $D$ ) and instability factor ( $F$ ) can be differentiated with respect to time for non-proportional loading:

$$\Delta D = \frac{n}{\varepsilon_f(\eta, \bar{\theta})} D^{(1-\frac{1}{n})} \Delta \varepsilon^{pl} \quad (2.4)$$

$$\Delta F = \frac{n}{\varepsilon_{crit}(\eta, \bar{\theta})} F^{(1-\frac{1}{n})} \Delta \varepsilon^{pl} \quad (2.5)$$

In Equations (2.4) and (2.5), the incremental damage and instability formulations serve as functions of the current damage factor and instability measure, respectively.  $\varepsilon_{crit}$  is the critical strain (i.e., equivalent plastic strain at the onset of necking) to serve as a weighting function of the actual stress state, and  $\Delta \varepsilon^{pl}$  is the incremental equivalent plastic strain. Generally defined at the onset of diffuse necking, the instability factor reaches unity so that accumulated damage initiates coupling to the stress tensor, and this allows for material softening by deriving the Lemaitre's classical principle of effective stress [44, 73]:

$$\sigma_m^* = \sigma_c (1 - D^*) \quad (2.6)$$

$$D^* = \begin{cases} 0 & \text{if } F < 1 \\ \left( \frac{D - D_{crit}}{1 - D_{crit}} \right)^m & \text{if } F = 1 \end{cases} \quad (2.7)$$

where  $\sigma_m^*$  is the modified stress coupled to damage,  $\sigma_c$  is the current stress, and  $D_{crit}$  is the critical threshold damage value corresponding to the unity instability factor.

Then, the modified stress can be calculated by:

$$\sigma^* = \sigma_c \left( 1 - \left( \frac{D - D_{crit}}{1 - D_{crit}} \right)^m \right) \text{ for } D \geq D_{crit} \quad (2.8)$$

where  $m$  is the fade exponent, which can be defined as a function of mesh sizes to govern the stress fading and control the energy dissipation.

### **2.2.2 Rationale of the GISSMO Implementation**

The GISSMO incorporates the effect of the stress triaxiality and Lode angle parameter to predict the onset of fracture of ductile materials [14–16]. In our study, the overall procedure to establish the GISSMO is displayed in Figure 2.1. In the GISSMO parameterization (see Section 2.3.1), designing and testing different geometries of specimens is to characterize the stress state of the material. Specifically, formulated by the equivalent plastic strain at fracture as a function of the stress triaxiality and Lode angle parameter, the fracture surface is to describe the fracture at different stress triaxialities with considerations for non-proportional strain paths [74]. The instability surface is established by the critical strain as a function of stress triaxiality and Lode angle parameter. It describes the appearance of necking and coupling initiation of the damage and stress tensor of the material under the non-proportional loading [75]. Next, in the GISSMO calibration (see Section 2.3.1), the damage exponent, fade exponent curve, mesh regularization curve, and strain rate scale curve are determined. The damage exponent allows for non-linear damage accumulation [15, 69]. The fade exponent governs the stress fading rate of the material and the post-necking behavior of the material until fracture (i.e., the rate of energy dissipation), which is defined as a function of mesh sizes [75]. The mesh regularization curve is used to regularize the fracture surface [74], energy dissipation over deformation [75], and update the damage and equivalent plastic strain calculated from the reference mesh size to the used mesh size by multiplying the mesh regularization factor [54, 70, 76]. This is needed to provide a similar fracture prediction when different mesh sizes are used [69, 74], which will improve consistency in fracture behavior realization. The governing equations are shown in the literature [54, 77] to further describe the work principles of mesh regularization in the GISSMO. The strain rate scale curve is established by the

normalized value as a function of strain rate to scale the fracture surface at different strain rates [66]. Then, we conduct the ballistic impact simulation to validate the calibrated GISSMO (see Section 2.3.2) and explore the structural design using the validated GISSMO (see Section 2.3.3 and 2.4).

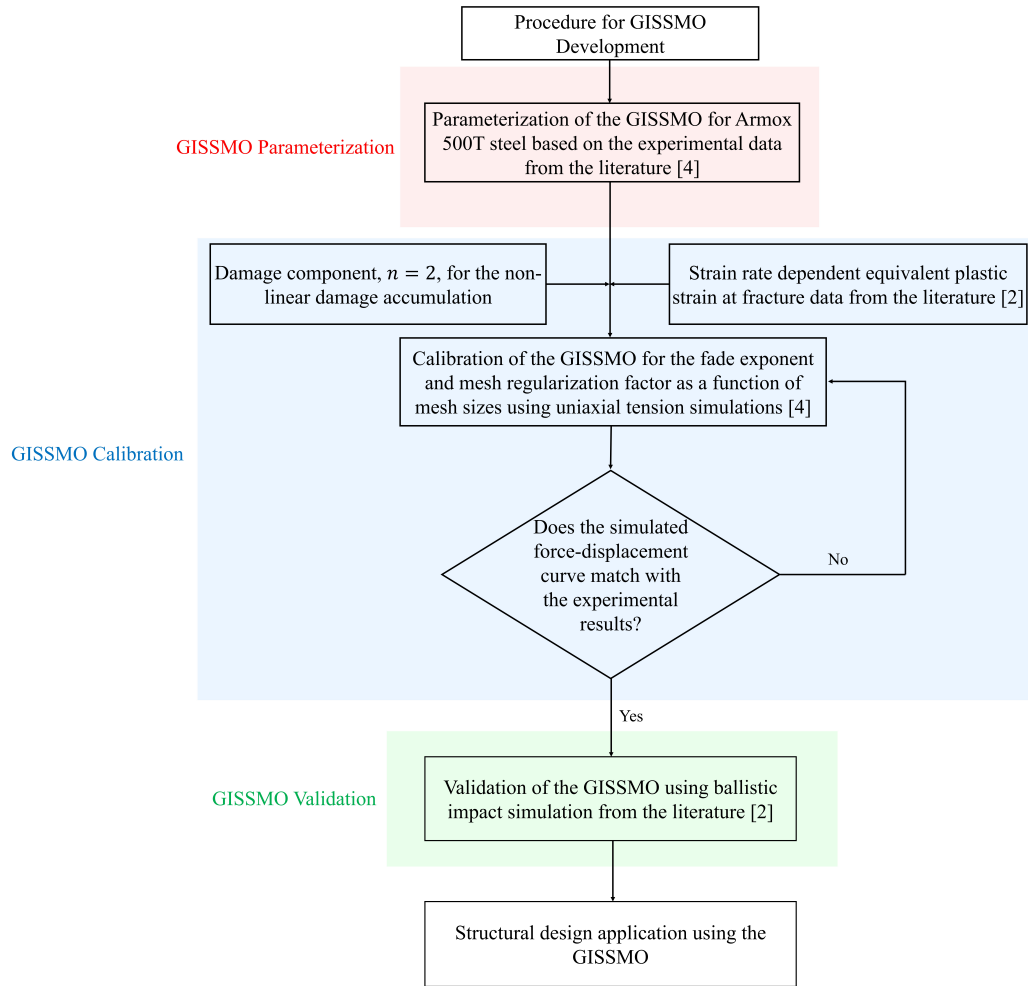


Figure 2.1: The flow chart for the GISSMO implementation.

## 2.3 Numerical Simulations with the GISSMO Implementation

This section demonstrates the GISSMO implementation in LS-DYNA applied for ballistic simulations with Armox 500T steel plates. Experimental and numerical data of Armox 500T steel from Popławski et al. [4] are used to determine the model parameters and calibrate the GISSMO. Experimental impact data from Iqbal et al. [2] is then used to validate the dynamic ballistic behavior of the Armox 500T steel subjected to impact by 12.7 mm and 7.62 mm projectiles. The validated model is then applied in high-velocity impact applications. In this study, the projectile and RHA backing are modeling using the Johnson-Cook model and constants from the literature [2, 78–80]. The Johnson-Cook model descriptions are documented in 4.1 since they are not the focus of this study.

### 2.3.1 Parameter Determination and Calibration for the GISSMO

The fracture surface and instability surface are determined for the Armox 500T steel using the data from Popławski et al. [4]. The fracture surface is formed to quantify the fracture initiation using the equivalent plastic strain at the moment of fracture in the stress space of the material [70]. The stress state of the material is defined based on the stress triaxiality and the Lode angle parameter. The stress triaxiality is positive in the tension state and negative when the material is under a compressive state. In addition, the Lode angle parameter ranges from -1, representing the state of axisymmetric compression, to 1, representing the state of axisymmetric tension, with details are provided in Rad et al. [81].

Figure 2.2 (a) shows the fracture surface of Armox 500T steel that is produced as the GISSMO input by using the data from Popławski et al. [4]. Motivated by the literature [4, 82], the biharmonic spline interpolation method is used in this study for generating the fracture surface in MATLAB [83]. Next, the instability surface (see

Figure 2.2 (b)) is constructed by initiating coupling of the damage to stress tensor for which the strain at the necking point is usually taken as the critical strain for a measure of instability [4, 55]. Note that the shear and compression state data is not included in the instability surface parameterization for Armox 500T steel since no physical necking phenomena occur on the conducted shear and compression experiments from the work done by Popławski et al. [4]. Then, surface discretization is conducted for both fracture and instability surfaces to generate incremental points using as GISSMO inputs into the LS-DYNA software. The DEFINE\_CURVE function is used to produce the equivalent plastic strain at fracture/critical strain and stress triaxiality curve for each Lode angle parameter value, and the DEFINE\_TABLE function is applied to construct the Lode angle parameter.

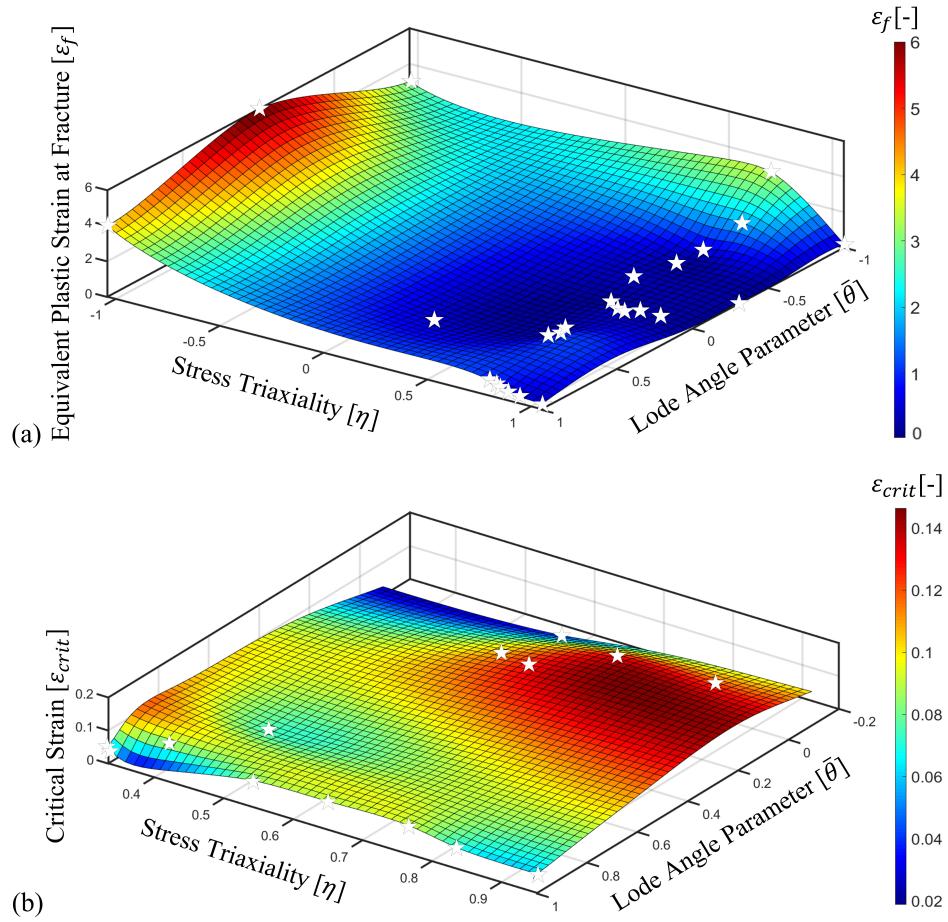


Figure 2.2: Parameterization of the GISSMO input surfaces: (a) fracture surface of the ArmoX 500T steel and (b) instability surface of the ArmoX 500T steel. The surfaces are produced using the biharmonic spline interpolation function in MATLAB based on the experimental data from Popławski et al. (2020) [4].

Next, before calibrating the GISSMO, two numerical settings consisting of the damage exponent and strain rate scale curve are required. In the GISSMO, the damage exponent is set to 2, allowing for non-linear damage accumulation, which is consistent with numerical settings from the literature [14, 69]. The effect of strain rate is necessary to be accounted for in the GISSMO framework to capture the responses of Armox 500T steel undergoing ballistic impact. In our study, the experimental equivalent plastic strains at fracture captured at different strain rates (0.0001/s to 1000/s) derived from the experimental data of Iqbal et al. [2] are used and implemented into the GISSMO. In Figure 2.3, the experimental data [2] is fitted using a first-degree polynomial equation with a determined 0.873 R-Square value ( $y = ax + b$ , where  $a = 0.069$  and  $b = 0.90$ ). Next, the experimental equivalent plastic strain at fracture at each strain rate is then normalized with respect to the value at a strain rate of 0.1/s. Hence, the normalized value as a function of strain rate is then implemented into the GISSMO for Armox 500T steel.

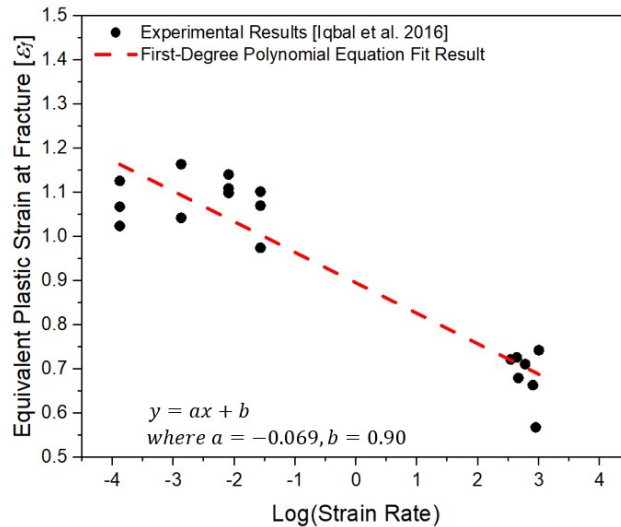


Figure 2.3: Equivalent plastic strain at fracture data from Iqbal et al. (2016) [2] used to account for strain rate effect into the established GISSMO.

Figure 2.4 shows the 1/8 symmetric finite element (FE) model used for the GISSMO calibration by reproducing uniaxial tension tests with the same geometries and dimensions as the experimental work done by Popławski et al. [4]. The von Mises

criterion-based model (MAT\_PIECEWISE\_LINEAR\_PLASTICITY [70]) serves as the strength model to describe the elastic-plastic behavior in Armox 500T steel. A hardening curve defines the true stress and plastic strain relation of Armox 500T steel, and the experimental data from the study of Popławski et al. [4] is used to parameterize our simulation parameters. The important parameters (density is  $7850 \text{ kg/m}^3$ , Young's modulus is  $207 \text{ GPa}$ , and Poisson's ratio is 0.3 [4]) are also defined in this strength model, and these are also taken from the study of Popławski et al. [4]. Then, the GISSMO serves as the fracture model to predict the fracture initiation of Armox 500T steel. The magnified view in Figure 2.4 indicates the FE model is controlled by symmetric plane boundaries. A constant strain rate of  $0.1/\text{s}$  is converted as the loading rate for representing a quasi-static condition [4]. The displacement controlled loading rate is assigned to the model in the positive x-axis direction. The FE model is meshed using the constant stress solid elements (ELFORM = 1), and these are controlled by the hourglass function (IQH = 4, QM = 0.03) in order to prevent the excitation of zero-energy degrees of freedom [70].

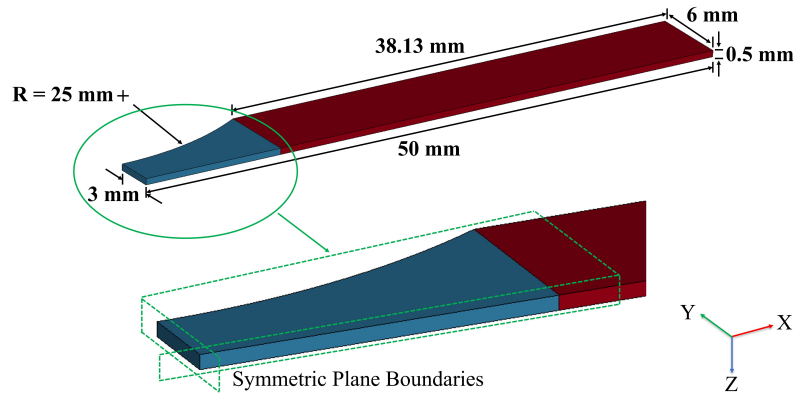


Figure 2.4: Tensile model configuration in LS-DYNA with symmetric boundary conditions used for the GISSMO calibration. Geometry and dimensions of the model are from Popławski et al. (2020) [4].

As shown in Figure 2.1, to calibrate the GISSMO, the fade exponent curve and mesh regularization curve are then determined using uniaxial tensile simulations, following works by Popławski et al. [4]. The different mesh sizes (i.e., 0.1 mm, 0.2

mm, 0.25 mm, 0.35 mm, and 0.5 mm) are used in the simulations. First, it is necessary to model the post-necking behavior of Armox 500T steel as it describes the procedure of stress-strain localization [84]. In our current study, the fade exponent is extracted by running iterative uniaxial tension simulations, and then matching the simulations with the experimental curves after the onset of necking at different mesh sizes. Second, Armox 500T steel has been shown to be sensitive to mesh size reported in the study done by Iqbal et. al [2], therefore, the mesh regularization function of the GISSMO is needed to reduce the mesh size dependency and improve computational efficiency in the simulation [77]. Hence, a larger mesh size determined from the established mesh regularization curve can be used in our ballistic impact simulations. In our study, the displacement-at-fracture at different mesh sizes is simulated to establish the mesh regularization curve as shown in Figure 2.5 (b).

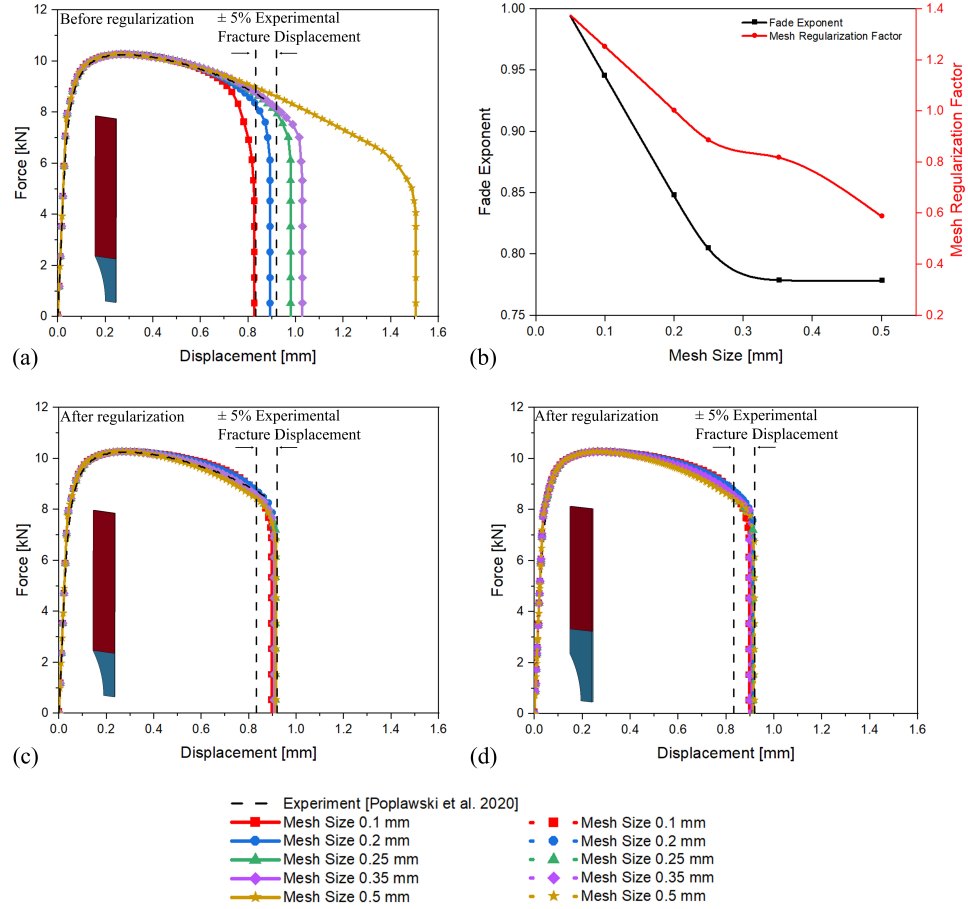


Figure 2.5: Force-displacement curve of numerical results for different element sizes plotted against experimental results from Popławski et al. (2020) [4]: (a) before applying the mesh regularization function, (b) fade and mesh regularization curve used in the GISSMO calibration, (c) after applying the mesh regularization function, and (d) comparison of numerical results for an alternative boundary condition with a smaller clamping area.

Figure 2.5 (a) shows the numerical force-displacement curve for different mesh sizes before applying the mesh regularization function. It is observed that the numerical force-displacement curve and experimental curve are in good agreement before the onset of necking. Once necking occurs, the numerical curve (i.e., fracture displacement) deviates from the experimental fracture displacement, and they are highly mesh-dependent. Figure 2.5 (b) shows the extracted fade exponent and the mesh regularization factor associated with each mesh size. The smoothing spline function in MATLAB is applied because it obtains the best-fit to the data points. Note that the mesh regularization factor is calculated based on the curve with a 0.2 mm mesh size because of its closeness to the experimental data and extrapolated to a 0.05 mm mesh size to cover the mesh size range from 0.05 mm to 0.5 mm [4]. The mesh regularization curve is constructed to allow simulated force-displacement using different mesh sizes in accordance with the experimental measurements. Next, Figure 2.5 (c) shows the regularized numerical force-displacement curves, and they are in good agreement with the experimental results after applying fade exponent and mesh regularization curves into the GISSMO. Lastly, Figure 2.5 (d) shows numerical results for an alternative boundary condition with a smaller clamping area, and the comparison results demonstrate that changing the boundary condition will not influence the calibration results. Altogether, the GISSMO is properly calibrated for further validations, and the 0.5 mm mesh size determined from the established mesh regularization curve can be used to model the Armox 500T steel plate in ballistic impact simulations.

### **2.3.2 GISSMO Validation**

The first validation case presents a 10 mm thick Armox 500T steel plate subjected to impact by a 12.7 mm armor piercing incendiary (API) projectile and uses data from Iqbal et al. [2] (see Experiment A and B in Table 2.1). The second validation case is conducted using an 8 mm thick Armox 500T steel plate subjected to impact by a 7.62 mm API projectile and uses data from Iqbal et al. [2] (see Experiment C

in Table 2.1). The third validation case aims to compare the results presented in the study of Iqbal et al. [2] with those of the ballistic limit and Recht-Ipson model [85] for a 10 mm thick Armox 500T steel plate.

First, Figure 2.6 shows the configuration of the FE model setup and dimensions of the target plate used as a high-velocity ballistic impact validation case. The Armox 500T steel target plate with a  $200 \text{ mm} \times 200 \text{ mm}$  span and a 10 mm thickness is impacted by a 12.7 mm API projectile at the plate center at velocities of 832 m/s and 842 m/s, following the work by Iqbal et al. [2]. The  $100 \text{ mm} \times 100 \text{ mm} \times 10 \text{ mm}$  impact site of the Armox 500T steel target is discretized with constant stress solid elements with a 0.5 mm element size and variable meshing in other locations is considered to reduce the computational cost. Figure 2.6 demonstrates the detailed geometry and dimensions of the deformable steel core of the 12.7 mm API projectile modeled using the JC model (see 4.1), which has 52.6 mm in total length, 10.9 mm in shank diameter, 7.65 mm in tail diameter, and 19.1 mm in nose length. The API projectile tip site is consistently meshed with a 0.5 mm element size. The hourglass control and artificial viscosity function are applied to the projectile (IHQ = 5, QM = 0.15, Q1 = 1.5, Q2 = 0.06) and ballistic target (IHQ = 4, QM = 0.03, Q1 = 1.5, Q2 = 0.06). Table 4.1 provides the JC strength and damage model parameters for the 12.7 mm API projectile corresponding to Mie–Grüneisen equations of state parameters from Kury et al. [86]. Following the recommendation of Iqbal et al. [2], the ERODING\_SURFACE\_TO\_SURFACE function is applied as the kinematic segment-based contact between the projectile served as the master segments and the target employed as the slave segments with a dynamic friction coefficient of 0.02 [87, 88]. The impact velocities of 832 m/s and 842 m/s with the positive x-axis direction are assigned to the projectile. The nodes in the periphery of the target are fixed in six degrees of freedom. The node at the rear center of the projectile is traced to measure the projectile residual velocity. Finally, in the second ballistic impact validation case from Iqbal et al. [2], the same Armox 500T steel plate mesh is used except that the

plate is now 8 mm thick. The 7.62 mm API projectile is modeled with a steel core, lead fillet, and copper jacket. The projectile impact velocity is 824 m/s, and the residual velocities given in Table 2.1 are compared with the results of Iqbal et al. [2] to confirm successful validation.

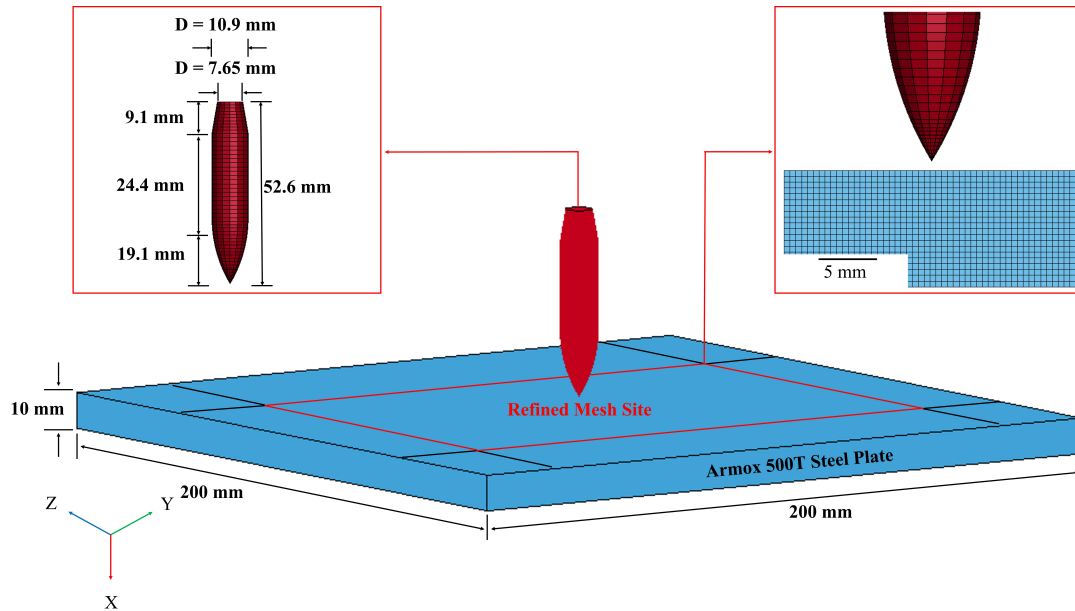


Figure 2.6: Numerical setups for ballistic impact of a 10 mm thick ArmoX 500T steel plate subjected to impact by the 12.7 mm armor piercing incendiary projectile. Geometries with dimensions are replicated from Iqbal et al. (2016) [2].

In the first two validation cases, Table 2.1 summarizes the experimental and simulated ballistic impact results comparing impact velocity, projectile residual velocity, and the percentage errors between numerical and experimental data [2]. It is observed that the final projectile residual velocity is within 3% error between the experimental data and numerical predictions, and this outperforms the JC model presented in Table 2.1. In addition, the typical impact failure behaviors after impact are also reproduced in LS-DYNA simulations, including the frontal spallation, a bulge at the back plate surface, and a circular hole on the target. A good agreement is found between the diameters of circular holes of 13.1 mm and 8.1 mm reported in the experiments [2], and 13.2 mm and 8.2 mm measured in the LS-DYNA simulations for Armox 500T steel plates subjected to impact by the 12.7 mm and 7.62 mm projectile, respectively.

In the last validation case, multiple impact velocities are employed as recommended by Iqbal et al. [2]. In the current study, the ballistic limit is determined to be 494 m/s, and this is in good agreement with the one reported in the study of 501 m/s [2]. The simulated results are then fitted using the least square method with a determined 0.998 R-Square value to calibrate the Recht-Ipson model parameters ( $a = 1.0$  and  $p = 1.94$ ) [85]. Figure 2.7 illustrates good agreement between the simulated projectile residual velocity and the results from Iqbal et al. [2] for a 10 mm thick plate impacted by a 12.7 mm API projectile. Overall, both qualitative observations (i.e., fracture behaviors with plate spalling and bulging) and quantitative measurements (e.g., projectile residual velocity and hole size after impact) confirm the GISSMO is validated and able to capture the impact response of the Armox 500T steel.

Table 2.1: Comparison of projectile residual velocity and perforation hole diameter between experimental ballistic results from Iqbal et al. (2016) [2] and LS-DYNA simulation results.

Ballistic Experiments	Impact Velocity [m/s]	Projectile Residual Velocity [m/s]	% Error	Reported Perforation Hole Diameter [mm]
Experiment A	832	664 (Simulation from [2]: 692)	4.2	Exp. Reported: 13.1
LS-DYNA Simulation	832	678	2.1	
Experiment B	842	686 (Simulation from [2]: 709)	3.4	Sim. Measured: 13.2
LS-DYNA Simulation	842	688	0.3	
Experiment C	824	334 (Simulation from [2]: 350)	4.8	Exp. Reported: 8.1
LS-DYNA Simulation	824	334	0.0	Sim. Measured: 8.2

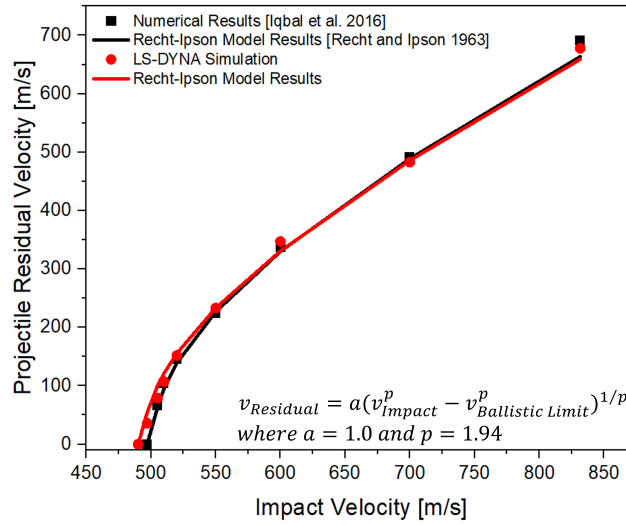


Figure 2.7: Comparison of projectile residual velocity in LS-DYNA simulation and numerical results from Iqbal et al. (2016) [2] and calculated results from the Recht–Ipson model [85].

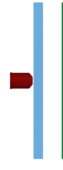
### 2.3.3 Numerical Setups of the Structural Design Application

This section demonstrates the application of the GISSMO in structural design by investigating the impact behaviors of a bi-layer plate system against a fragment simulating projectile (FSP) using the LS-DYNA hydrocode. The roles of the standoff distance and impact angle of obliquity on the performance of the steel armor system are explored in this section. Table 2.2 shows the four configurations and numerical setups implemented in this study. Specifically, the 20 mm FSP with the mass of 54.5 grams is used to simulate the features of fragmentation during penetration of a multi-layered target [89]. The bi-layer systems consist of a 10 mm thick Armox 500T steel front plate and a 12.7 mm thick RHA back plate. Following the assumption of Iqbal et al. [2] and to prevent the damage of the plates interfering with the boundary, 200 mm  $\times$  200 mm targets are created and weigh 7.13 kg. The 20 mm standoff distance is chosen to allow enough space between plates to prevent bulging of the front plate interfering with the back plate [36]. The 30-degree inclined angle and the impact velocity of 1000 m/s are selected to prevent projectile sliding from the front plate and to allow the front plate to be fully penetrated, respectively.

Figure 2.8 shows the model configuration in ballistic simulations. Specifically, the constant stress type element with the size of 0.5 mm is consistently used to discretize the 100 mm  $\times$  100 mm impact site of front and back plates. The hourglass control (IHQ = 4, QM = 0.03) and artificial viscosity (Q1 = 1.5 and Q2 = 0.06) function are used for both plates. The validated GISSMO is used to model the Armox 500T steel plate and Table 4.2 provides the JC model parameters for the RHA plate associated with the Mie–Grüneisen equations of state parameters from the study by Kohn et al. [90]. Note that the JC strength model parameters are taken based on the 3-20 mm thickness of the RHA class 1 plate in the study done by Neuberger et al. [78]. The JC damage model parameters of the RHA are obtained from work by Johnson and Cook [42], and this set of damage parameters are also used in the Joo et al. study [91].

Moreover, the geometries with dimensions of the 20 mm FSP follow the standard from MIL-DTL-46593B (MR) [92]. To maintain consistency, the shank site of the projectile is also meshed with an element size of 0.5 mm and controlled by hourglass and artificial viscosity functions ( $IHQ = 4$ ,  $QM = 0.03$ ,  $Q1 = 1.5$ ,  $Q2 = 0.06$ ). Table 4.2 also provides the JC model parameters for the 4340 steel FSP given by Ng et al. [79] and Serjouei et al. [80] and Mie–Grüneisen equations of state parameters from work by Thurber et al. [93]. In addition, following the recommendation of Iqbal et al. [2], the nodes in the periphery of both plates are fixed, and the kinematic segment-based `ERODING SURFACE_TO_SURFACE` contact is used between the projectile (serving as the master segments) and the targets (employed as the slave segments) with a dynamic friction coefficient of 0.02 [87, 88]. The static friction coefficient of 0.5 in the `AUTOMATIC SURFACE_TO_SURFACE` contact setting is suggested if the plates are in-contact [34].

Table 2.2: Impact configurations to investigate the role of the standoff distance and angle of obliquity on the ballistic performance of the steel armor system. The maximum depth of penetration for a 12.7 mm thick RHA plate, minimum RHA plate thickness required to stop the projectile, and mass of the bi-layer plates are compared for the different noted impact configurations.

	Configuration	Standoff Distance	Inclined Angle	Maximum Depth of Penetration	Minimum RHA Plate Thickness	Mass of Bi-layer Plates
Configuration 1		0 mm	0 deg	7.80 mm	4.70 mm	4.61 kg
Configuration 2		20 mm	0 deg	8.29 mm	4.75 mm	4.63 kg
Configuration 3		0 mm	30 deg	4.57 mm	3.50 mm	4.24 kg
Configuration 4		20 mm	30 deg	5.08 mm	4.00 mm	4.40 kg

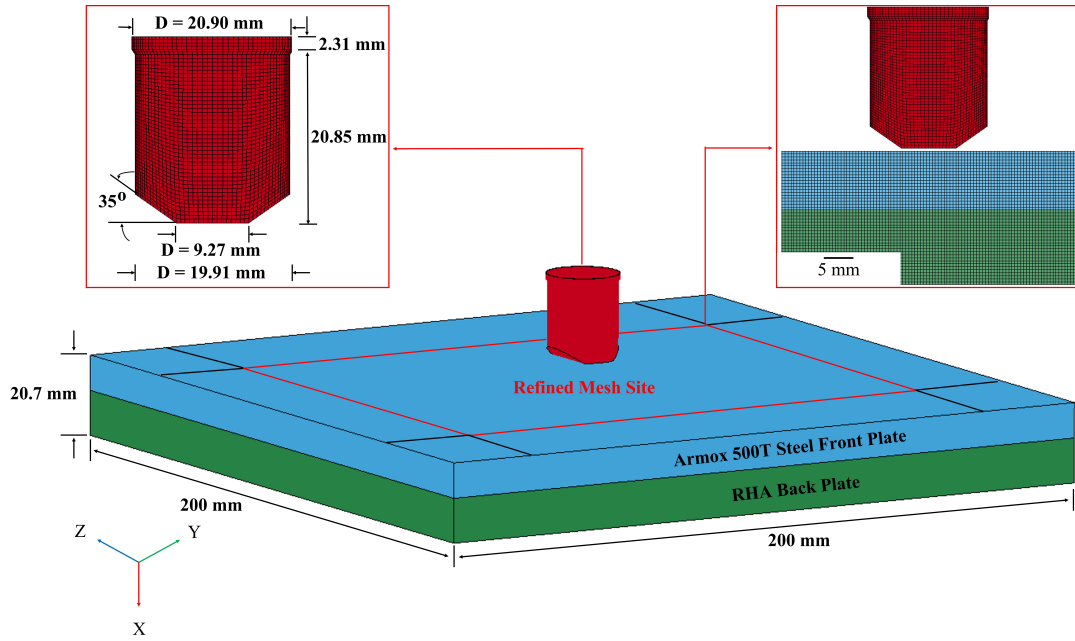


Figure 2.8: Ballistic simulation configuration consisting of a 10 mm thick Armox 500T steel front plate and 12.7 mm thick RHA back plate with no standoff distance under a normal impact from a 20 mm fragment simulating projectile. Geometries of the FSP are replicated from MIL-DTL-46593B (MR) [92].

## 2.4 Results and Discussion

This section explores the role of selected standoff distances and impact angles of obliquity on the resulting ballistic performance of bi-layered armor systems impacted by a fragment simulating projectile. In this study, the maximum depth of penetration (DOP), minimum thickness for the RHA back plate required to stop the projectile, and failure modes on different impact configurations are compared across the different bi-layer system configurations (defined previously in Table 2.2).

### 2.4.1 Impact Failure Behaviors of Bi-Layered Steel Systems

This sub-section describes the impact failure behaviors of Armox 500T steel front plate and RHA back plate bi-layer systems (see Figure 2.8). Figure 2.9 shows the projectile kinetic energy as a function of time with corresponding insets at noted time instances showing the impact behavior of a system consisting of a 10 mm thick Armox 500T steel front plate and 12.7 mm thick RHA back plate. Figure 2.9 (a) represents the bi-layered steel system under a normal impact from a FSP. The key findings include: (1) compared to the plates with a 20 mm standoff distance (i.e., Configuration 2), a greater decrease in the rate of the projectile kinetic energy is found for the in-contact steel system (i.e., Configuration 1), and this may be related to impact phenomena such as a greater global deformation of the front plate, the back plate withstanding the deformation of the front plate, and in-contact plate promoting energy dissipation [30], (2) from the insets (i.e., Figure 2.9 (a1) and (a2)), the interference of the in-contact plates results in a greater deformation of the front plate in Figure 2.9 (a1) than its in Figure 2.9 (a2), and this is similar to the observations in Dey et al. [30], and (3) a greater deformation is observed in the projectile for the in-contact systems, and the projectile has the typical mushrooming behaviors that are consistent with experimental and simulated observations in the literature [94, 95].

Figure 2.9 (b) shows the bi-layered steel system under a 30 deg oblique impact

from a FSP. Compared to plates with a 20 mm standoff distance in Figure 2.9 (a2) and (b2), the projectile kinetic energy for a 30 deg impact angle has a more rapid decrease during penetration into the front plate. This can be explained by noting the thickness of the plate in the impact direction (i.e., normal to the 30-degree impact angle) is larger when compared to the thickness in the normal impact direction, for which will further reduce the projectile kinetic energy. From the insets (i.e., Figure 2.9 (b1) and (b2)) showing the global impact behaviors of the steel plate system under a normal impact, the bulging of the back plate is observed but much less while compared to the steel plate system under an oblique impact shown in Figure 2.9 (a1) and (a2). This is explained by: (1) larger size of the ejected debris can be observed from the projectile after the impact, and the back plate withstands the impact from the projectile with less kinetic energy. Similar observations are found in the literature [96, 97], (2) the yaw of the projectile affects deformations of the back plate and results in lower penetration depth [98], and (3) after fully penetrating the front plate, the projectile significantly deflects, and this reduces its ability to further penetrate the back plate. Lastly, it is observed that the projectile kinetic energy has a more rapid decrease for the plates at normal impact in Figure 2.9 (a) than the plates at oblique impact in Figure 2.9 (b), and this may be related to the observed phenomena such as a greater deformation of the projectile and a considerable amount of energy conversion from the kinetic energy of the projectile to rotational kinetic energy at oblique impact [99].

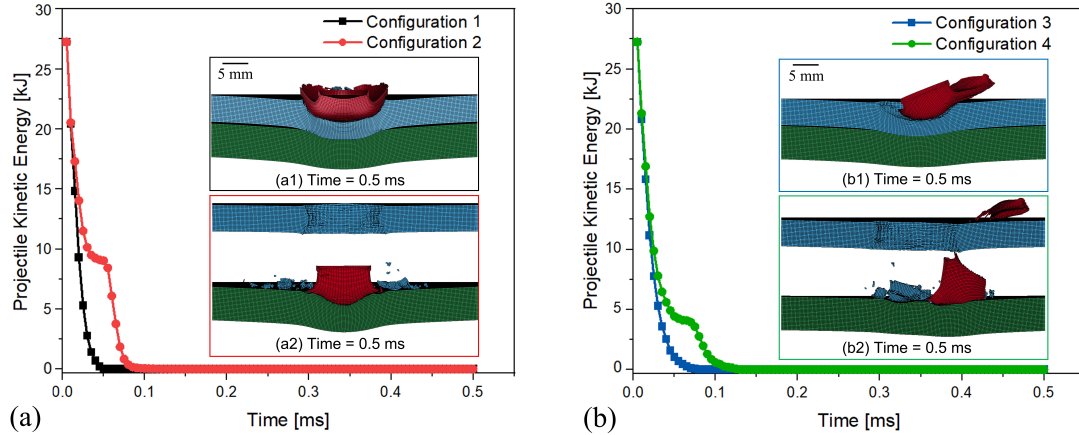


Figure 2.9: Projectile kinetic energy plotted against time with corresponding impact failure behaviors at noted time instances for a configuration of a 10 mm thick Armox 500T steel front plate and 12.7 mm thick RHA back plate impacted by a FSP at 1000 m/s: (a1) plates with no standoff distance under a normal impact and (a2) plates with a 20 mm standoff distance under a normal impact, and (b1) plates with no standoff distance under a 30 deg oblique impact and (b2) plates with a 20 mm standoff distance under a 30 deg oblique impact.

Table 2.2 shows the measured maximum depth of penetration (DOP) results of the four configurations with a 10 mm thick Armox 500T steel backed with a 12.7 mm RHA steel. Here, the DOP values for each impact configuration are measured from the deepest position of the keyhole in the plate produced by the projectile. From Table 2.2, it is observed that: (1) the lowest DOP value occurs for the in-contact bi-layer plate under a 30 deg oblique impact from a FSP, (2) the highest DOP value is observed at a 20 mm standoff distance between the plates, and this is related to the greater plate deformation caused by the projectile and frontal plate fragments that are observed in Figure 2.9 (a), and (3) with the Armox 500T steel being 10 mm, the minimum thickness of the RHA back plate is the smallest and largest for the third and second configuration, respectively.

Figure 2.10 presents the typical impact failure behaviors of the bi-layered steel system and the FSP at noted time instances for the four configurations. Here, the Armox 500T front plate thickness is 10 mm and the RHA back plate thickness is chosen as the minimum thickness required to stop the projectile ( $v=0$  m/s) for a

given configuration (thicknesses noted in Table 2.2). Results on Configuration 1 (i.e., Figure 2.10 (a)) and Configuration 2 (i.e., Figure 2.10 (b)) are compared to investigate the typical impact failure behaviors of the plates under a normal impact from a FSP, and Configuration 3 (i.e., Figure 2.10 (c)) and Configuration 4 (i.e., Figure 2.10 (d)) are compared to study the impact failure behaviors of the plates under a 30 deg oblique impact from a FSP. A 0.025 ms time for the in-contact plates is selected for visualization as this corresponds to when the front plate being completely penetrated. A 0.065 ms time for the plates with a 20 mm standoff distance is selected for visualization for when the projectile and frontal plate fragments reach to the back plate.

The key observations as shown in Figure 2.10 include: (1) at noted time instances, larger sizes of the plugs by Armox 500T steel and RHA plates are observed in Configuration 1 than Configuration 2, and this is similar to experimental observations in Dolinski and Rittel [100], from which plugging failure is caused by stretching deformation during penetration [36]. In Figure 2.10 (a), the sizes of plugs from the front and back plates are similar because the plug formation of the back plate is mainly contributed by the frontal plug, (2) in Figure 2.10 (b), a reduced diameter plug is formed and ejected from the back plate, and this is attributed by stretching thinning and necking in the tensile zone, where the fracture strain cannot be achieved in necking region [36], (3) in Figure 2.10 (a) and (b), it is observed that the Armox 500T steel plate has a greater deformation [30]. This has similar observations in the literature [101, 102], (4) a greater global deformation of Armox 500T steel plate has been observed for the in-contact plates than the one for the plates with a 20 mm standoff distance. This is consistent with the experimental observation in the literature [30], (5) in Figure 2.10 (c), the hole size of the back plate is similar to the plug size ejected from the front plate because material failure is caused by bending deformation, and (6) overall, we see the basic impact failure behaviors of plug formation [102, 103], separation [102], frontal spallation [104], shear dominated fracture [105, 106], and bulging

of the plates [107] in Configurations 1 and 2. Finally, impact failure behaviors of the bi-layered steel system under a 30 deg oblique impact from a FSP in Configuration 3 (i.e., Figure 2.10 (c)) and Configuration 4 (i.e., Figure 2.10 (d)) involve petaling [108, 109], plugging [110, 111], and vertical cut mode [112, 113]. Specifically, larger plugs results in larger petals and larger structural deformations of the RHA plate when comparing Configurations 3 and 4. Importantly, the yaw behavior of the projectile is more significant under oblique impact simulations (Configurations 3 and 4) than normal impacts (Configurations 1 and 2), and this will be explored quantitatively later.

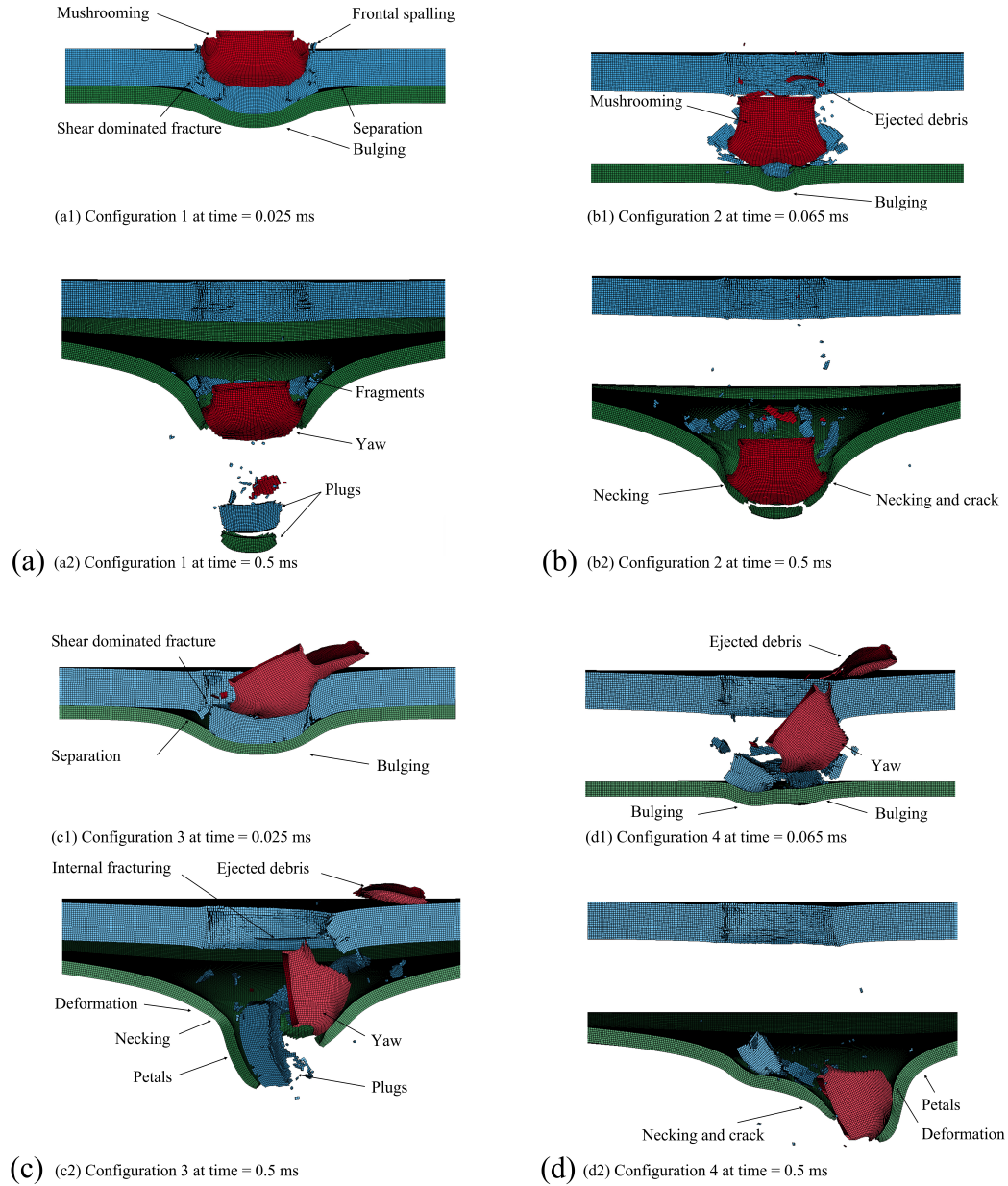


Figure 2.10: Impact failure behaviors at noted time instances for different configurations for a 1000 m/s impact from a fragment simulating projectile: (a) Configuration 1, (b) Configuration 2, (c) Configuration 3, and (d) Configuration 4. Configurations 1 and 2 shows plug formation as the dominant impact failure mechanism. Larger size of plugs are formed and observed in Configuration 1 than Configuration 2 as the projectile penetrates. The basic impact failure behaviors of the plates impacted by the FSP can be identified as frontal spallation, shear dominated fracture, delamination of layers, and bulging of the plates. Moreover, the failure behaviors of Configurations 3 and 4 involves petaling and plugging. It is observed that larger plugs results in larger petals and larger structural deformations of the RHA plate in Configuration 3.

## 2.4.2 Impact Failure Behaviour of the Projectile

This sub-section explores the yaw and deflection of the projectile to better understand results from Figure 2.9 to Figure 2.10. Here, for the four configurations, the Armox 500T steel front plate thickness is 10 mm and the RHA back plate thickness is chosen as the minimum thickness required to stop the projectile ( $v = 0$  m/s and thicknesses for a given configuration noted are in Table 2.2). The yaw is measured by tracing the deflection angle from the mid-sectional plane of the projectile through discrete points in projectile displacement. Figure 2.11 also shows the residual velocity of the projectile plotted against time with insets associated with the deformed projectiles at noted time instances. The colors shown in Figure 2.11 correspond to the four impact configurations from Table 2.2. The key findings include: (1) the projectile has a similar behavior (i.e., a small increase rate of yaw angles) among four configurations at the projectile displacement of 30 mm. Then, the projectile yaw angle in Configuration 3 rapidly increases at a small increment of the projectile displacement. A similar trend in Configuration 4 is observed once the projectile reaches to the back plate, (2) larger yaw angles are measured for Configurations 3 and 4 when compared to Configurations 1 and 2. This is attributed to impact failure behaviors such as plugging and petaling (observed previously in Figure 2.10), and normal impact has less effects on changes of the yaw angle of the projectile. Observations and discussions are consistent with the literature [103, 114–117], and (3) oblique impact can not only significantly increase the yaw angle but also deformed projectile, which has larger corrosion and debris ejection, and this is consistent with a similar experimental observation in the study by Gee and Littlefield [118]. The significant changes in yaw angle, larger corrosion and debris ejection are attributed to the thickness of the plate in the impact direction of the projectile being thicker than for a normal impact when the projectile impacts the target at an angle (i.e., Configurations 3 and 4).

### 2.4.3 The Role of Standoff Distance and Angle of Obliquity on Ballistic Responses of the Bi-Layered Steel Systems

This final sub-section discusses the role of standoff distance and angle of obliquity on ballistic responses of the Armox 500T steel and RHA by a FSP. The numerical simulations are conducted based on a 10 mm thick Armox 500T steel front plate and a 3 mm thick RHA back plate. A 3 mm thick RHA back plate is selected to allow the RHA back plate to be fully penetrated and the JC model parameters in Table 4.2 is suitable to use for 3 - 20 mm thickness of the RHA plate. Figure 2.12 shows the residual velocity of the projectile as a function of time. The insets show impact failure behaviors at noted time instances for the four impact configurations (labeled in color) defined in Table 2.2. A 0.5 ms time is selected based on when the projectile completely penetrates the RHA back plate. The node at the rear center of the projectile is traced to measure the residual velocity of the projectile. From Figure 2.12, the key findings include: (1) the final projectile residual velocities are similar in magnitude between the in-contact (i.e., Configuration 1) and plates with a 20 mm standoff distance (i.e., Configuration 2) under a normal impact from a FSP, and this is because of the high projectile impact velocity and insignificant yaw behavior of the projectile, (2) a larger residual velocity of the projectile difference is found in the plates undergoing a 30 deg oblique impact regardless of its in-contact (i.e., Configuration 3) and 20 mm standoff distance (i.e., Configuration 4). Altogether, the standoff distance has a slight influence on projectile residual velocity for the plates under a normal impact from a FSP but a significant effect for the plates under a 30 deg oblique impact. It is believed that the standoff distance and angle of obliquity magnify the yaw behavior of the projectile for a 30 deg impact angle. Hence, the projectile has significant yaw that greatly decreases the impact energy transmission from the projectile to plates, resulting in the lower residual velocity of the projectile, and (3) it is also observed that final projectile residual velocities of Configurations 2 and 4 are greater than Configurations 1 and 3, respectively, indicating that the

in-contact plate systems have a better ballistic resistance than the plates with a standoff distance, and this is consistent with the literature [33, 114, 119]. Overall, Configuration 3 (i.e., the plates with no standoff distance under an oblique impact) is considered to be best performing among the selected configurations because of lowest DOP value, smallest thickness of the RHA back plate, and lowest residual velocity.

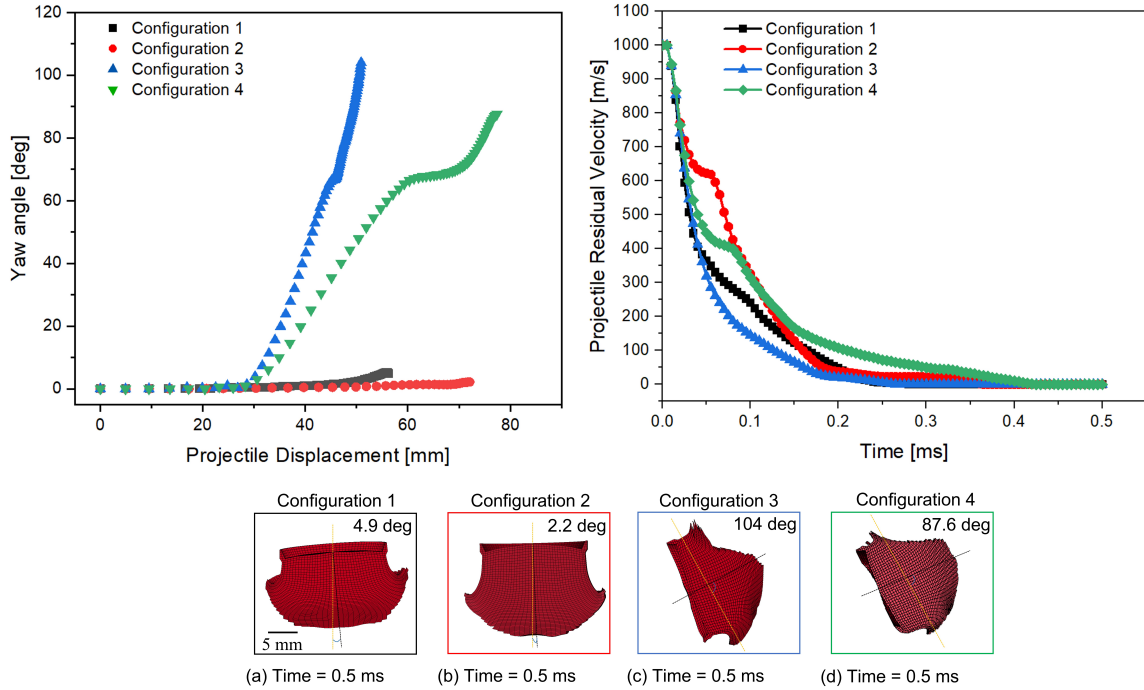


Figure 2.11: Projectile yaw angle plotted against projectile displacement and projectile residual velocity plotted against time with corresponding insets of the deformed projectiles at noted time instances for a 1000 m/s impact from a fragment simulating projectile: (a) Configuration 1, (b) Configuration 2, (c) Configuration 3, and (d) Configuration 4. The four configurations consist of the 10 mm thick ArmoX 500T steel front plate and the RHA back plate with the minimum thickness required to stop the projectile ( $v = 0$  m/s and thicknesses for a given configuration noted in Table 2.2). A large yaw angle is measured for Configurations 3 and 4, and this indicates the angle of obliquity could lead to greater resulting time-evolved yaw angles. Comparing Configurations 1 and 2, and 3 and 4, the angle of obliquity has more effects on the changes of the deflection angle of the projectile than the standoff distance.

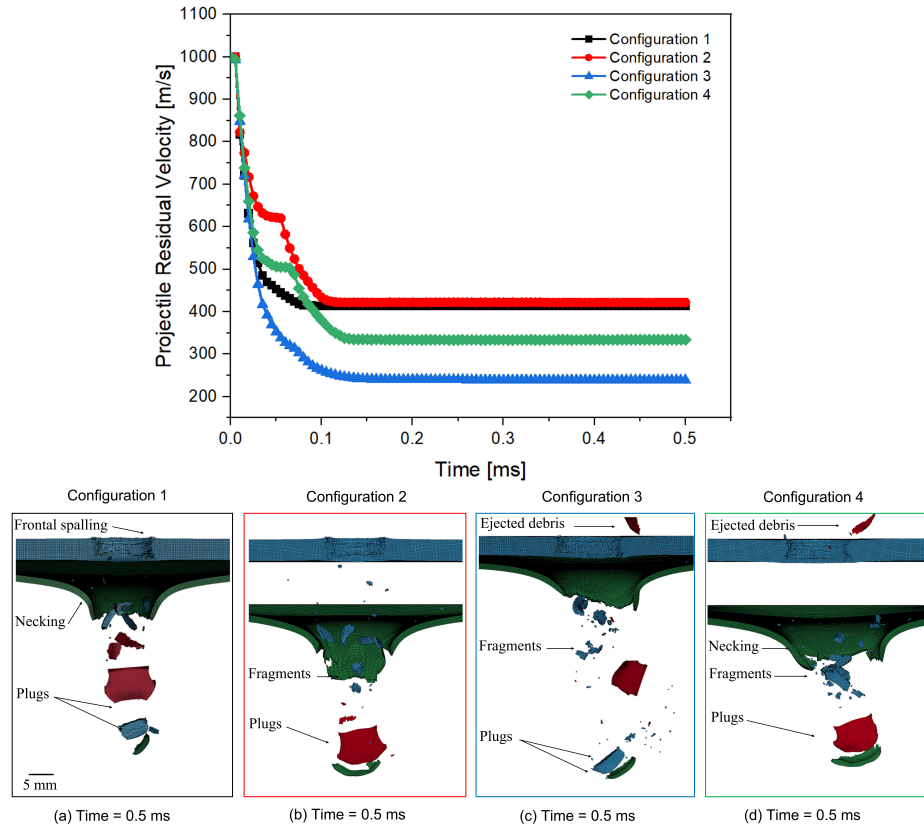


Figure 2.12: Projectile residual velocity plotted against time for a 10 mm thick ArmoX 500T steel front plate and a 3 mm thick RHA back plate with corresponding failure modes at noted time instances for a 1000 m/s impact from a fragment simulating projectile: (a) plates with no standoff distance under a normal impact, (b) plates with a 20 mm standoff distance under a normal impact, (c) plates with no standoff distance under a 30 deg oblique impact, and (d) plates with a 20 mm standoff distance under a 30 deg oblique impact. It is observed that final projectile residual velocities of Configurations 2 and 4 are greater than Configurations 1 and 3, respectively, and this indicates the in-contact plate system has a better ballistic resistance than the plates with a standoff distance.

## 2.5 Conclusions

This study investigates the fracture-mechanical behavior of Armox 500T steel through the computational finite element framework from the LS-DYNA explicit solver. The Generalized Incremental Stress State dependent damage MOdel (GISSMO), incorporating the stress state-dependent behavior of the material and the effect of strain rate, is implemented in the uniaxial tension [4] and ballistic impact simulations [2]. A good agreement between the ballistic experimental and numerical results demonstrates the implemented GISSMO offers good predictions on the fracture behaviors (e.g., spalling and bulging) and quantitative measurements (e.g., projectile residual velocity and hole size after impact) for Armox 500T steel [2]. The mesh regularization reduces the mesh size dependency and improves the computational efficiency of ballistic impact simulations [120], which can be shown in Section 2.3.1 and 4.2. Once validated, the GISSMO is used in a structural-scale design application by simulating a bi-layer steel system impacted by a 20 mm fragment simulating projectile (FSP). From simulated results, the implemented GISSMO enables the failure mechanisms of Armox 500T steel to be captured, such as plug formation [100, 102], frontal spallation [104], shear dominated fracture [106], and petaling [108]. The key findings of the structural design are summarized below:

- (1) The lowest values on the maximum depth of penetration and minimum thickness for the RHA back plate to stop the projectile are congruent and the overall results demonstrate that plates with no standoff distance under a 30 deg oblique impact from a FSP offer the best ballistic performance.

- (2) Through impact failure behaviors for four configurations, the plug formation, frontal spallation, shear dominated fracture, and bulging of the plate are observed. Large sizes of plugs are observed for the plates with no standoff distance under a normal and 30 deg oblique impact from a FSP. The petaling behavior of plates mainly occurs in plates with no standoff distance and a 20 mm standoff distance under a 30

deg oblique impact from a FSP.

(3) A large increase of the projectile yaw and deflection are observed and measured from plates with no standoff distance and a 20 mm standoff distance under a 30 deg oblique impact from a FSP compared with the normal impact, and this is attributed to the petaling behavior of the plates and thickness difference of the RHA plate related to four impact configurations. Normal impact has less effects on the yaw behavior of the projectile. More projectile erosion and debris ejection are observed in the plates under a 30 deg oblique impact, and this is attributed to the thickness of the plate relative to the impact direction of the projectile.

(4) The final projectile residual velocity obtained are similar for the plates under a normal impact but there is a significant difference for the plates under a 30 deg oblique impact. This demonstrates that the standoff distance has a larger influence on projectile residual velocity when the FSP impacts the plate at an oblique angle of 30 deg. The lowest value of the projectile residual velocity is obtained with the plates with no standoff distance, demonstrating that this impact configuration has the best ballistic performing against a FSP under the simulated conditions in the current study.

(5) As potential future work, it is recommended to parameterize the instability surface of Armox 500T steel by designing, for example, hat-shaped specimens from work done by Herzig et al. [121] to characterize the negative value range of stress triaxiality ( $-1 < \eta < 0$ ) and Lode angle parameter ( $-1 < \bar{\theta} < 0$ ) for Armox 500T steel. In addition, experiments at elevated temperatures could also be performed and temperature-dependent properties incorporated into the GISSMO formulation [120].

# Chapter 3

## Conclusion and Future Works

### 3.1 Implications

Conclusively, this thesis developed a stress state- and strain rate-dependent fracture model, explored the impact failure behaviors of Armox 500T steel, and provided future guidance for designs of Armox 500T steel-based hybrid armor system. The main contributions of this thesis are summarized below:

1. This thesis models the impact failure behavior of Armox 500T steel under the high-velocity ballistic impact by implementing the Generalized Incremental Stress State dependent damage MOdel (GISSMO) in LS-DYNA/Explicit software. The two important numerical inputs of the GISSMO (i.e., fade exponent and mesh regularization curves) are determined for Armox 500T steel. The strain rate effect is addressed in the GISSMO, which enables capturing the fracture initiation of Armox 500T steel undergoing dynamic impacts. For the first time in the literature, the GISSMO has been implemented to predict the ballistic impact behaviors (e.g., spalling and bulging) and responses (e.g., projectile residual velocity and hole size after impact) of Armox 500T steel.
2. This thesis provides new capabilities and insights (e.g., the minimum thickness of RHA backing layer in a bi-layered Armox 500T steel/RHA system and the effect of standoff distance on the yaw behavior of the projectile) into the design

of lightweight and high-performing Armox 500T steel-based armor structures for light armored vehicles. In a bi-layered Armox 500T steel/RHA system, the minimum thickness of the RHA back plate required to stop the projectile is determined for four impact configurations. Specifically, the thickness of RHA back plate is 4.70 mm and 4.75 mm for the impact configuration with 0 mm and 20 mm standoff distance under 0 deg impact, respectively, and its 3.50 mm and 4.00 mm for the impact configuration with 0 mm and 20 mm standoff distance under 60 deg impact, respectively. The role of 0 mm and 20 mm standoff distances and 0 deg and 60 deg impact angles of obliquity of the projectile on the resulting ballistic performance of a bi-layered armor system are explored. Specifically, adding the 20 mm standoff distance reduces the yaw angle of the projectile for both 0 deg and 60 deg impact. In addition, an in-contact plate system has a better ballistic resistance than the plates with a 20 mm standoff distance. Overall, the impact configuration of the plates with no standoff distance under a 60 deg oblique impact is considered to be the best performing among the selected configurations.

## 3.2 Future Work and Recommendations

Based on the current thesis study, the recommended future work includes:

- *Stress state characterization of Armox 500T steel* - The current instability surface of Armox 500T steel is not characterized at negative stress triaxiality and Lode angle parameter. As potential future work, it is recommended to parameterize the instability surface of Armox 500T steel by designing, for example, hat-shaped specimens following work done by Herzig et al. [121] to provide the negative value range of stress triaxiality ( $-1 < \eta < 0$ ) and Lode angle parameter ( $-1 < \bar{\theta} < 0$ ) for Armox 500T steel.
- *Considering strain rate- and temperature-dependency into the GISSMO* - The

current GISSMO has the strain rate scale function to capture the fracture initiation of Armox 500T steel under the high strain rate impact. However, the thermal effect is not addressed in the current implemented GISSMO. To well-introduce these effects into the GISSMO and quantify the fracture initiation, experiments at different strain rates [2] and elevated temperatures [120] could be performed for each designed experimental sample. Altogether, the strain rate- and temperature-dependent properties (i.e., fracture surface at different strain rates and temperatures) are then incorporated into the GISSMO formulation.

- *Equi-biaxial dome test* - Equi-biaxial dome tests can help to develop a better understanding of strain localization of Armox 500T steel under complex stress conditions, and are used for the GISSMO refinement and validation. As inspired by Rahmaan et al. [69], the equi-biaxial dome test can be used to define the stress state of Armox 500T steel at a negative value range of stress triaxiality and used for the GISSMO calibration in terms of fade exponent curve and mesh regularization curve. Therefore, a larger mesh size (e.g.,  $\geq 5$  mm mesh size ) can be used for large-scale model simulations.
- *Average stress triaxiality and Lode angle parameter to establish fracture surface of Armox 500T steel* - The stress triaxiality and Lode angle parameter are not always constant from the undeformed stage up to fracture of Armox 500T steel [51]. As inspired by Bao and Wierzbicki [122], the following equations can be used to calculate average stress triaxiality and Lode angle parameter, which can be then used to establish fracture surface of Armox 500T steel (i.e., equivalent plastic strain at fracture as a function of average stress triaxiality and average Lode angle parameter).

$$\eta_{average} = \frac{1}{\varepsilon_f} \int_0^{\varepsilon_f} \eta d\varepsilon \quad (3.1)$$

$$\bar{\theta}_{average} = \frac{1}{\varepsilon_f} \int_0^{\varepsilon_f} \bar{\theta} d\varepsilon \quad (3.2)$$

where  $\varepsilon_f$  is equivalent plastic strain at fracture,  $\varepsilon$  is equivalent plastic strain,  $\eta$  is stress triaxiality,  $\eta_{average}$  is average value of stress triaxiality,  $\bar{\theta}$  is Lode angle parameter, and  $\bar{\theta}_{average}$  is average value of Lode angle parameter.

# Bibliography

- [1] “Armox 500T general product data sheet,” *SSAB*, 2017.
- [2] M. Iqbal, K. Senthil, P. Sharma, and N. Gupta, “An investigation of the constitutive behavior of Armox 500T steel and armor piercing incendiary projectile material,” *International Journal of Impact Engineering*, vol. 96, pp. 146–164, 2016.
- [3] M. Saleh, M. M. Kariem, V. Luzin, K. Toppler, H. Li, and D. Ruan, “High strain rate deformation of Armox 500T and effects on texture development using neutron diffraction techniques and SHPB testing,” *Materials Science and Engineering: A*, vol. 709, pp. 30–39, 2018.
- [4] A. Popławski, P. Kedzierski, and A. Morka, “Identification of Armox 500T steel failure properties in the modeling of perforation problems,” *Materials Design*, vol. 190, p. 108 536, 2020.
- [5] M. Saleh, V. Luzin, M. Kariem, and D. Ruan, “Analysis of the residual stress in Armox 500T armour steel and numerical study of the resultant ballistic performance,” (2016).
- [6] M. Saleh, V. Luzin, M. Kariem, K. Thorogood, and D. Ruan, “Experimental measurements of residual stress in Armox 500T and evaluation of the resultant ballistic performance,” 2019.
- [7] Z. Mohammad, P. K. Gupta, A. Baqi, and M. A. Iqbal, “Energy dissipation characteristics of single curvature metallic shells subjected to ballistic impact,” *European Journal of Mechanics - A/Solids*, vol. 89, p. 104 279, 2021.
- [8] P. Kedzierski, A. Morka, G. Sławiński, and T. Niezgoda, “Optimization of two-component armour,” *Bulletin of the Polish Academy of Sciences Technical Sciences*, vol. 63, 2015.
- [9] I. Polyzois and G. Toussaint, “Fracture characterization of AlgoTuf 400F steel for simulating blast damage,” *Scientific Report*, no. DRDC-RDDC-2020-R070 — Scientific Report, 2020.
- [10] Y. Bai and T. Wierzbicki, “A new model of metal plasticity and fracture with pressure and lode dependence,” *International Journal of Plasticity*, vol. 24, no. 6, pp. 1071–1096, 2008.

- [11] L. Xue and T. Wierzbicki, “Ductile fracture initiation and propagation modeling using damage plasticity theory,” *Engineering Fracture Mechanics*, vol. 75, no. 11, pp. 3276–3293, 2008.
- [12] Y. Deng, A. Hu, X. Xiao, and B. Jia, “Experimental and numerical investigation on the ballistic resistance of ZK61m magnesium alloy plates struck by blunt and ogival projectiles,” *International Journal of Impact Engineering*, vol. 158, p. 104021, 2021.
- [13] X. Liu, S. Yan, K. J. Rasmussen, and G. G. Deierlein, “Experimental investigation of the effect of lode angle on fracture initiation of steels,” *Engineering Fracture Mechanics*, vol. 271, p. 108637, 2022.
- [14] F. Neukamm, M. Feucht, K. Roll, and A. Haufe, “On closing the constitutive gap between forming and crash simulation,” May (2008).
- [15] F. Neukamm, A. Haufe, and M. Feucht, “Consistent damage modelling in the process chain of forming to crashworthiness simulations,” Sep. (2008).
- [16] M. Basaran, D. Weichert, S. D. Wölkerling, M. Feucht, and F. Neukamm, “An extension of the GISSMO damage model based on Lode angle dependence,” (2010).
- [17] A. Paman, G. Sukumar, B Ramakrishna, and V. Madhu, “An optimization scheme for a multilayer armour module against 7.62 mm armour piercing projectile,” *International Journal of Protective Structures*, vol. 11, no. 2, pp. 185–208, 2020.
- [18] K. Senthil and M. A. Iqbal, “Prediction of superior target layer configuration of armour steel, mild steel and aluminium 7075-T651 alloy against 7.62 AP projectile,” *Structures*, 2020.
- [19] S. Dikshit, V. Kutumbarao, and G. Sundararajan, “The influence of plate hardness on the ballistic penetration of thick steel plates,” *International Journal of Impact Engineering*, vol. 16, no. 2, pp. 293–320, 1995.
- [20] Z. Rosenberg and E. Dekel, “A computational study of the relations between material properties of long-rod penetrators and their ballistic performance,” *International Journal of Impact Engineering*, vol. 21, no. 4, pp. 283–296, 1998.
- [21] C. Lo, H. Li, G. Toussaint, and J. D. Hogan, “On the evaluation of mechanical properties and ballistic performance of two variants of boron carbide,” *International Journal of Impact Engineering*, vol. 152, p. 103846, 2021.
- [22] Y. Wang, X. Chen, X. Xiao, V. V. Vershinin, R. Ge, and D. Li, “Effect of lode angle incorporation into a fracture criterion in predicting the ballistic resistance of 2024-T351 aluminum alloy plates struck by cylindrical projectiles with different nose shapes,” *International Journal of Impact Engineering*, vol. 139, p. 103498, 2020.

- [23] Y. Deng, H. Wu, Y. Zhang, X. Huang, X. Xiao, and Y. Lv, “Experimental and numerical study on the ballistic resistance of 6061-T651 aluminum alloy thin plates struck by different nose shapes of projectiles,” *International Journal of Impact Engineering*, vol. 160, p. 104 083, 2022.
- [24] J. Hetherington and P. Lemieux, “The effect of obliquity on the ballistic performance of two component composite armours,” *International Journal of Impact Engineering*, vol. 15, no. 2, pp. 131–137, 1994.
- [25] M. Iqbal, K. Senthil, V. Madhu, and N. Gupta, “Oblique impact on single, layered and spaced mild steel targets by 7.62 AP projectiles,” *International Journal of Impact Engineering*, vol. 110, pp. 26–38, 2017.
- [26] S. Signetti and A. Heine, “Transition regime between high-velocity and hypervelocity impact in metals – a review of the relevant phenomena for material modeling in ballistic impact studies,” *International Journal of Impact Engineering*, vol. 167, p. 104 213, 2022.
- [27] R. Corran, P. Shadbolt, and C. Ruiz, “Impact loading of plates — an experimental investigation,” *International Journal of Impact Engineering*, vol. 1, no. 1, pp. 3–22, 1983.
- [28] J. Radin and W. Goldsmith, “Normal projectile penetration and perforation of layered targets,” *International Journal of Impact Engineering*, vol. 7, no. 2, pp. 229–259, 1988.
- [29] X. Teng, S. Dey, T. Børvik, and T. Wierzbicki, “Protection performance of double-layered metal shields against projectile impact,” *Journal of Mechanics of Materials and Structures - J MECH MATER STRUCT*, vol. 2, pp. 1309–1329, Sep. 2007.
- [30] S. Dey, T. Børvik, X. Teng, T. Wierzbicki, and O. Hopperstad, “On the ballistic resistance of double-layered steel plates: An experimental and numerical investigation,” *International Journal of Solids and Structures*, vol. 44, no. 20, pp. 6701–6723, 2007.
- [31] J. K. Holmen, O. S. Hopperstad, and T. Børvik, “Low-velocity impact on multi-layered dual-phase steel plates,” *International Journal of Impact Engineering*, vol. 78, pp. 161–177, 2015.
- [32] G. Ben-Dor, A. Dubinsky, and T. Elperin, “Effect of air gaps on the ballistic resistance of ductile shields perforated by nonconical impactors,” *Journal of Mechanics of Materials and Structures*, vol. 1, pp. 279–299, Jun. 2006.
- [33] A. Alavi Nia and G. Hoseini, “Experimental study of perforation of multi-layered targets by hemispherical-nosed projectiles,” *Materials Design*, vol. 32, no. 2, pp. 1057–1065, 2011.
- [34] M. Iqbal, P. Gupta, V. Deore, S. Tak, G. Tiwari, and N. Gupta, “Effect of target span and configuration on the ballistic limit,” *International Journal of Impact Engineering*, vol. 42, pp. 11–24, 2012.

- [35] Z. Wei, D. Yunfei, C. Z. Sheng, and W. Gang, “Experimental investigation on the ballistic performance of monolithic and layered metal plates subjected to impact by blunt rigid projectiles,” *International Journal of Impact Engineering*, vol. 49, pp. 115–129, 2012.
- [36] Y. Deng, W. Zhang, and Z. Cao, “Experimental investigation on the ballistic resistance of monolithic and multi-layered plates against hemispherical-nosed projectiles impact,” *Materials Design*, vol. 41, pp. 266–281, 2012.
- [37] J. Cui, R. Ye, N. Zhao, J. Wu, and M. Wang, “Assessment on energy absorption of double layered and sandwich plates under ballistic impact,” *Thin-Walled Structures*, vol. 130, pp. 520–534, 2018.
- [38] V. Tvergaard and A. Needleman, “Analysis of the cup-cone fracture in a round tensile bar,” *Acta Metallurgica*, vol. 32, no. 1, pp. 157–169, 1984.
- [39] A. Olinger, C. Foster, and J. Wilkerson, “Homogenized modeling of anisotropic impact damage in rolled AZ31B with aligned second-phase particles,” *Journal of Dynamic Behavior of Materials*, vol. 6, pp. 445–458, 2020.
- [40] S. Sayahlatifi, C. Shao, A. McDonald, and J. Hogan, “3D microstructure-based finite element simulation of cold-sprayed Al-Al<sub>2</sub>O<sub>3</sub> composite coatings under quasi-static compression and indentation loading,” *Journal of Thermal Spray Technology*, vol. 31, pp. 102–118, 2022.
- [41] G. Johnson and W. Cook, “A constitutive model and data for metals subjected to large strains, high strain rates and high temperatures,” in *Proceedings of the 7th International Symposium on Ballistics*, vol. 21, The Hague, The Netherlands, (1983), pp. 541–547.
- [42] G. Johnson and W. Cook, “Fracture characteristics of three metals subjected to various strains, strain rates, temperatures and pressures,” *Engineering Fracture Mechanics*, vol. 21, no. 1, pp. 31–48, 1985.
- [43] F. J. Zerilli and R. W. Armstrong, “Dislocation-mechanics-based constitutive relations for material dynamics calculations,” *Engineering Failure Analysis*, vol. 61, pp. 1816–1825, 1987.
- [44] J. Lemaitre, “A continuous damage mechanics model for ductile fracture,” *Journal of Engineering Materials and Technology*, vol. 107, no. 1, pp. 83–89, Jan. 1985.
- [45] M. Nilsson, “Constitutive model for Armox 500T and Armox 600T at low and medium strain rates,” *Weapons and protection SE-147/25*, 2003.
- [46] P. Skoglund, M. Nilsson, and A. Tjernberg, “Fracture modelling of a high performance armour steel,” *J. Phys. IV France*, vol. 134, pp. 197–202, 2006.
- [47] M. Rezasefat, T. Mirzababaie Mostofi, and T. Ozbakkaloglu, “Repeated localized impulsive loading on monolithic and multi-layered metallic plates,” *Thin-Walled Structures*, vol. 144, p. 106332, 2019.

- [48] P. Ranaweera, D. Weerasinghe, P. Fernando, S. N. Raman, and D. Mohotti, “Ballistic performance of multi-metal systems,” *International Journal of Protective Structures*, vol. 11, no. 33, pp. 379–410, 2020.
- [49] K. Senthil and M. Iqbal, “Prediction of superior target layer configuration of armour steel, mild steel and aluminium 7075-T651 alloy against 7.62 AP projectile,” *Structures*, vol. 29, pp. 2106–2119, 2021.
- [50] A. Saxena *et al.*, “A comparative numerical analysis on the effect of welding consumables on the ballistic resistance of smaw joints of armor steel,” *Applied Sciences*, vol. 11, no. 8, 2021.
- [51] F. Andrade, M. Feucht, and A. Haufe, “On the prediction of material failure in LS-DYNA: A comparison between GISSMO and DIEM,” Jun. (2014).
- [52] J. Effelsberg, A. Haufe, M. Feucht, F. Neukamm, and P. Dubois, “On parameter identification for the GISSMO damage model,” Oct. (2012).
- [53] A. Zhumagulov, “Crashworthiness and material characterization of multi-cellular AA6063 extrusions,” *UWSpace*, 2017.
- [54] M. Dai, L. Ying, S. Wang, H. Ma, P. Hu, and Y. Wang, “Modeling the crashworthiness analysis of functional graded strength thin-walled structure with phenomenological GISSMO model,” *Thin-Walled Structures*, vol. 180, p. 109 766, 2022.
- [55] L. Pérez Caro, M. Schill, K. Haller, E.-L. Odenberger, and M. Oldenburg, “Damage and fracture during sheet-metal forming of alloy 718,” *International Journal of Material Forming*, vol. 13, 2020.
- [56] M. Otroshi, M. Rossel, and G. Meschut, “Stress state dependent damage modeling of self-pierce riveting process simulation using GISSMO damage model,” *Journal of Advanced Joining Processes*, vol. 1, p. 100 015, 2020.
- [57] Z. Xue *et al.*, “Equivalent characterization of pre-strained material properties and mechanical behavior prediction of steel/aluminum self-piercing riveted joints,” *Thin-Walled Structures*, vol. 182, p. 110 243, 2023.
- [58] N. Novak, M. Vesenjajk, L. Krstulović-Opara, and Z. Ren, “Mechanical characterisation of auxetic cellular structures built from inverted tetrapods,” *Composite Structures*, vol. 196, pp. 96–107, 2018.
- [59] S. Tabacu and C. Ducu, “Numerical investigations of 3D printed structures under compressive loads using damage and fracture criterion: Experiments, parameter identification, and validation,” *Extreme Mechanics Letters*, vol. 39, p. 100 775, 2020.
- [60] N. Novak, L. Starčević, M. Vesenjajk, and Z. Ren, “Blast response study of the sandwich composite panels with 3D chiral auxetic core,” *Composite Structures*, vol. 210, pp. 167–178, 2019.

- [61] J. Schlosser, S. Mouchtar, W. Rimkus, and R. Schneider, “Design optimisation of a side impact beam made out of high strength aluminium alloys using BARLAT YLD2000 and GISSMO failure model for the ”extended hotforming process”,” May (2019).
- [62] B. C. Cerik and J. Choung, “Rate-dependent combined necking and fracture model for predicting ductile fracture with shell elements at high strain rates,” *International Journal of Impact Engineering*, vol. 146, p. 103 697, 2020.
- [63] O. Orhan and A. Özel, “Homogenized pouch cell material modelling and a comparison study,” *International Journal of Energy Research*, vol. 45, no. 2, pp. 2668–2679, 2021.
- [64] N. J. Edwards, S. J. Cimpoeeru, N. Herzig, and D. Ruan, “Ballistic impact of flat-ended projectiles against 2024-T351 plate: Experiments and modeling,” *Journal of Aerospace Engineering*, vol. 35, no. 1, p. 04 021 124, 2022.
- [65] Q. Zhou, Z. Yao, C. Xu, D. Zhou, W. Liu, and L. Li, “Shared mechanism between flow drill screw and friction stir welding and its impact on failure prediction of steel-aluminum joints,” *Journal of Materials Processing Technology*, vol. 311, p. 117 796, 2023.
- [66] F. Rickhey, T. Park, and S. Hong, “Damage prediction in thermoplastics under impact loading using a strain rate-dependent gissmo,” *Engineering Failure Analysis*, vol. 149, p. 107 246, 2023.
- [67] D. Anderson, C. Butcher, N. Pathak, and M. Worswick, “Failure parameter identification and validation for a dual-phase 780 steel sheet,” *International Journal of Solids and Structures*, vol. 124, pp. 89–107, 2017.
- [68] P. Li, Q. Fan, X. Zhu, and H. Gong, “Study of high-speed-impact-induced conoidal fracture of ti alloy layer in composite armor plate composed of ti and al-alloy layers,” *Defence Technology*, vol. 17, no. 4, pp. 1434–1443, 2021.
- [69] T. Rahmaan, C. Butcher, S. Kim, and M. J. Worswick, “Characterization and prediction of fracture in 6000- and 7000-series aluminum alloy sheet under various stress states,” *Thin-Walled Structures*, vol. 173, p. 108 958, 2022.
- [70] *Livermore Software Technology Corporation (LSTC), LS-Dyna Keyword-Users Manual Volume II: Material Model. LS-DYNA R11*, 2019.
- [71] T Børvik, O. Hopperstad, T Berstad, and M Langseth, “A computational model of viscoplasticity and ductile damage for impact and penetration,” *European Journal of Mechanics - A/Solids*, vol. 20, no. 5, pp. 685–712, 2001.
- [72] K. Danas and P. Ponte Castañeda, “Influence of the Lode parameter and the stress triaxiality on the failure of elasto-plastic porous materials,” *International Journal of Solids and Structures*, vol. 49, no. 11, pp. 1325–1342, 2012.
- [73] J Lemaitre, *A Course on Damage Mechanics*. (1996).
- [74] F. Andrade, M. Feucht, and A. Haufe, “On the prediction of material failure in ls-dyna: A comparison between GISSMO and DIEM,” (2014).

- [75] F. Neukamm, M. Feucht, and A. Haufe, “Considering damage history in crash-worthiness simulations,” May 2009.
- [76] D.-Y. Kim, Y. Han, S. Shin, and H. Yook, “Numerical fracture analysis considering forming effect and element size regularization for automotive seat structures,” *SAE International journal of engines*, vol. 10, 287–295, 2017.
- [77] F. Andrade, M. Feucht, A. Haufe, and F. Neukamm, “An incremental stress state dependent damage model for ductile failure prediction,” *International Journal of Fracture*, vol. 200, 127–150, 2016.
- [78] A. Neuberger, S. Peles, and D. Rittel, “Scaling the response of circular plates subjected to large and close-range spherical explosions. part i: Air-blast loading,” *International Journal of Impact Engineering*, vol. 34, no. 5, pp. 859–873, 2007.
- [79] E. G. Ng, T. I. E. Wardany, and M. D. M. A. Elbestawi, “Physics-based simulation of high speed machining,” *Machining Science and Technology*, vol. 6, no. 3, pp. 301–329, 2002.
- [80] A. Serjouei, R. Chi, Z. Zhang, and I. Sridhar, “Experimental validation of blv model on bi-layer ceramic-metal armor,” *International Journal of Impact Engineering*, vol. 77, pp. 30–41, 2015.
- [81] S. G. Rad and A. Zajkani, “On the stress state-based coupled plasticity – ductile damage model for aluminum alloys considering the influence of high-rate impulsive preload,” *International Journal of Impact Engineering*, vol. 146, p. 103 715, 2020.
- [82] D. T. Sandwell, “Biharmonic spline interpolation of GEOS-3 and SEASAT altimeter data,” *Geophysical Research Letters*, vol. 14, no. 2, pp. 139–142, 1987.
- [83] MATLAB, *version 7.10.0 (R2010a)*. Natick, Massachusetts: The MathWorks Inc., 2010.
- [84] A. Sancho, M. Cox, T. Cartwright, C. Davies, P. Hooper, and J.P., “An experimental methodology to characterise post-necking behaviour and quantify ductile damage accumulation in isotropic materials,” *International Journal of Solids and Structures*, vol. 176-177, pp. 191–206, 2019.
- [85] R. F. Recht and T. W. Ipson, “Ballistic Perforation Dynamics,” *Journal of Applied Mechanics*, vol. 30, no. 3, pp. 384–390, Sep. 1963.
- [86] J. Kury, R Breithaupt, and C. Tarver, “Detonation waves in trinitrotoluene,” *Shock Waves*, vol. 9, pp. 227–237, 1999.
- [87] T. Børvik, S. Dey, and A. Clausen, “Perforation resistance of five different high-strength steel plates subjected to small-arms projectiles,” *International Journal of Impact Engineering*, vol. 36, no. 7, pp. 948–964, 2009.
- [88] T. Børvik, L. Olovsson, S. Dey, and M. Langseth, “Normal and oblique impact of small arms bullets on AA6082-T4 aluminium protective plates,” *International Journal of Impact Engineering*, vol. 38, no. 7, pp. 577–589, 2011.

- [89] G. Kechagiadakis and M. Pirlot, “Assessing the performance of personal protective equipment1,” in *Mine Action*, C. Beumier, D. Closson, V. Lacroix, N. Milisavljevic, and Y. Yvinec, Eds., Rijeka: IntechOpen, 2017, ch. 8.
- [90] B. J. Kohn, “Compilation of hugoniot equations of state,” (1969).
- [91] J. H. Joo, C. H. Lee, and J. H. Choi, “A numerical research on the penetration into a semi-infinite rolled homogeneous armor by a medium-caliber kinetic energy projectile,” in *Explosion, Shock Wave and High-Energy Reaction Phenomena*, ser. Materials Science Forum, vol. 673, Mar. (2011), pp. 197–202.
- [92] “MIL-DTL-46593B (MR), Projectile, calibers .22, .30, .50, and 20 mm fragment-simulating,” *Aberdeen Proving Ground (MD): Army Research Laboratory (2008)*,
- [93] A. J. Thurber, ““investigations of Hypervelocity Impact Physics” (2014).,” *Doctoral Dissertations. 15977.*,
- [94] M. Grujicic, B. Pandurangan, K. Koudela, and B. Cheeseman, “A computational analysis of the ballistic performance of light-weight hybrid composite armors,” *Applied Surface Science*, vol. 253, no. 2, pp. 730–745, 2006.
- [95] T. Frasn, L. Colard, E. Lach, A. Rusinek, and B. Reck, “Thick AA7020-T651 plates under ballistic impact of fragment-simulating projectiles,” *International Journal of Impact Engineering*, vol. 86, pp. 336–353, 2015.
- [96] W. Lee, H.-J. Lee, and H. Shin, “Ricochet of a tungsten heavy alloy long-rod projectile from deformable steel plates,” *Journal of Physics D: Applied Physics*, vol. 35, p. 2676, Oct. 2002.
- [97] J. Liu, Y. Long, and C. Ji, “Ballistic performance study on the finite steel target subjected to normal and oblique impact by copper explosively formed projectile,” *International Journal of Protective Structures*, vol. 9, no. 4, pp. 461–483, 2018.
- [98] Y. Vayig and Z. Rosenberg, “The effect of yaw on the penetration of rigid rods,” *International Journal of Impact Engineering*, vol. 148, p. 103 748, 2021.
- [99] T. Stergiou, K. P. Baxevanakis, A. Roy, and V. V. Silberschmidt, “Mechanics of ballistic impact with non-axisymmetric projectiles on thin aluminium targets. part II: Energy considerations,” *Engineering Failure Analysis*, vol. 143, p. 106 818, 2023.
- [100] M. Dolinski and D. Rittel, “Experiments and modeling of ballistic penetration using an energy failure criterion,” *Journal of the Mechanics and Physics of Solids*, vol. 83, pp. 1–18, 2015.
- [101] D. Tria and R. Trebiński, “Methodology for experimental verification of steel armour impact modelling,” *International Journal of Impact Engineering*, vol. 100, pp. 102–116, 2017.
- [102] P. Ranaweera, M. Bambach, D. Weerasinghe, and D. Mohotti, “Ballistic impact response of monolithic steel and tri-metallic steel–titanium–aluminium armour to nonrigid NATO FMJ M80 projectiles,” *Thin-Walled Structures*, vol. 182, p. 110 200, 2023.

- [103] L. Li *et al.*, “A laboratory experimental technique for simulating combined blast and impact loading,” *International Journal of Impact Engineering*, vol. 134, p. 103 382, 2019.
- [104] E. Flores-Johnson, M. Saleh, and L. Edwards, “Ballistic performance of multi-layered metallic plates impacted by a 7.62-mm APM2 projectile,” *International Journal of Impact Engineering*, vol. 38, no. 12, pp. 1022–1032, 2011.
- [105] J. Han *et al.*, “Experimental and numerical investigation on the ballistic resistance of 2024-T351 aluminum alloy plates with various thicknesses struck by blunt projectiles,” *International Journal of Impact Engineering*, vol. 163, p. 104 182, 2022.
- [106] R. Yu *et al.*, “Dynamic response of fully-clamped steel plate under laboratory-simulated sequential fragment impact and blast loading,” *Thin-Walled Structures*, vol. 182, p. 110 144, 2023.
- [107] T. Børvik, M. Langseth, O. Hopperstad, and K. Malo, “Ballistic penetration of steel plates,” *International Journal of Impact Engineering*, vol. 22, no. 9, pp. 855–886, 1999.
- [108] A. Rusinek, J. Rodríguez-Martínez, R. Zaera, J. Klepaczko, A. Arias, and C. Sauvelet, “Experimental and numerical study on the perforation process of mild steel sheets subjected to perpendicular impact by hemispherical projectiles,” *International Journal of Impact Engineering*, vol. 36, no. 4, pp. 565–587, 2009.
- [109] A. Gilioli, A. Manes, M. Giglio, and T. Wierzbicki, “Predicting ballistic impact failure of aluminium 6061-T6 with the rate-independent Bao–Wierzbicki fracture model,” *International Journal of Impact Engineering*, vol. 76, pp. 207–220, 2015.
- [110] A. Kane, T. Børvik, O. S. Hopperstad, and M. Langseth, “Finite element analysis of plugging failure in steel plates struck by blunt projectiles,” *Journal of Applied Mechanics*, vol. 76, no. 5, 2009.
- [111] P. Jena, N. Jagtap, K. Siva Kumar, and T. Balakrishna Bhat, “Some experimental studies on angle effect in penetration,” *International Journal of Impact Engineering*, vol. 37, no. 5, pp. 489–501, 2010.
- [112] Z. Mohammad, P. K. Gupta, and A. Baqi, “Experimental and numerical investigations on the behavior of thin metallic plate targets subjected to ballistic impact,” *International Journal of Impact Engineering*, vol. 146, p. 103 717, 2020.
- [113] T. Stergiou *et al.*, “Mechanics of ballistic impact with non-axisymmetric projectiles on thin aluminium targets. part i: Failure mechanisms,” *Engineering Failure Analysis*, p. 107 152, 2023.
- [114] C. Ji, L. Chen, Y. Long, and Q. Xu, “Dynamic behaviors of multi-layered steel targets with air gaps subjected to the impact of EFP simulants,” *International Journal of Protective Structures*, vol. 6, no. 1, pp. 65–80, 2015.

- [115] J. K. Holmen, J. K. Solberg, O. S. Hopperstad, and T. Børvik, “Ballistic impact of layered and case-hardened steel plates,” *International Journal of Impact Engineering*, vol. 110, pp. 4–14, 2017, Special Issue in honor of Seventy Fifth Birthday of Professor N. K. Gupta.
- [116] T. Fras, C. C. Roth, and D. Mohr, “Fracture of high-strength armor steel under impact loading,” *International Journal of Impact Engineering*, vol. 111, pp. 147–164, 2018.
- [117] H. Wei, X. Zhang, C. Liu, W. Xiong, H. Chen, and M. Tan, “Oblique penetration of ogive-nosed projectile into aluminum alloy targets,” *International Journal of Impact Engineering*, vol. 148, p. 103745, 2021.
- [118] D. Gee and D. Littlefield, “Yaw impact of rod projectiles,” *International Journal of Impact Engineering*, vol. 26, no. 1, pp. 211–220, 2001.
- [119] B. Ramakrishna, “Numerical studies on perforation of multi-layered targets by hemispherical-nosed projectiles,” *IOSR Journal of Mechanical and Civil Engineering*, vol. 11, pp. 80–94, 2014.
- [120] A. A. Camberg, T. Erhart, and T. Tröster, “A generalized stress state and temperature dependent damage indicator framework for ductile failure prediction in heat-assisted forming operations,” *Materials*, vol. 14, no. 17, 2021.
- [121] N. Herzig, S. Abdel-Malek, L. Meyer, and S. Cimpoeru, “Modeling of ductile failure in high strength steel,” *Procedia Engineering*, vol. 197, pp. 285–293, 2017.
- [122] Y. Bao and T. Wierzbicki, “On fracture locus in the equivalent strain and stress triaxiality space,” *International journal of mechanical sciences*, vol. 46, no. 1, pp. 81–98, 2004.
- [123] A. Haufe, M. Feucht, F. Neukamm, P. Dubois, and T. Borvall, *Damage and failure models for steel materials in the process chain of forming-to-crash in LS-DYNA*, 2012.

# Chapter 4

## Appendix

### 4.1 Constitutive Model Description

#### 4.1.1 Johnson-Cook Material Model

The Johnson-Cook (JC) model (MAT\_JOHNSON\_COOK) is employed to model the 7.62 mm and 12.7 mm armor piercing incendiary projectiles [2] (see Figure 2.6), fragment simulating projectile (FSP) [79, 80] and rolled homogeneous armor (RHA) steel back plate [42, 78] (see Figure 2.8). The corresponding model properties and constants are presented in Table 4.1 and Table 4.2.

The JC strength model [41] describes the flow stress,  $\bar{\sigma}$ , of the material based on the von Mises plasticity, as shown in Equation (A4.1).

$$\bar{\sigma} = [A + B (\varepsilon^{pl})^n] \left[ 1 + C \ln \frac{\dot{\varepsilon}^{pl}}{\dot{\varepsilon}_0} \right] \left[ 1 - \left( \frac{T_c - T_{room}}{T_m - T_{room}} \right)^m \right] \quad (\text{A4.1})$$

where material constants,  $A$ ,  $B$ ,  $C$ ,  $n$ , and  $m$  are well introduced by Johnson and Cook [41]. In Equation (A4.1),  $\varepsilon^{pl}$  is the equivalent plastic strain,  $\dot{\varepsilon}^{pl}$  is the equivalent plastic strain rate,  $\dot{\varepsilon}_0$  is the strain rate at the reference state,  $T_c$  is the current working temperature,  $T_m$  is the melting temperature, and  $T_{room}$  is the room temperature. Here, the first term defines the strain hardening, the second term accounts for the effect of the strain rate on yield stress in a normalized form, and the third term describes the temperature effect on the material deformation.

In addition, the JC damage model [42] is employed to predict material responses

subjected to external loads, and its fracture criterion defines damage in a linear accumulated level ( $n=1$  in Equation (2.4)) [56, 123]. The equivalent plastic strain at fracture is defined as a multiplicative function of stress triaxiality, strain rate, and temperature [42].

$$\varepsilon_f = [D_1 + D_2 e^{D_3 \eta}] \left[ 1 + D_4 \ln \frac{\dot{\varepsilon}^{pl}}{\dot{\varepsilon}_0} \right] \left[ 1 + D_5 \left( \frac{T_c - T_{room}}{T_m - T_{room}} \right) \right] \quad (\text{A4.2})$$

where  $D_1$  to  $D_5$  are damage parameters. In this study, the model constants for the RHA [42, 78] in Table 4.2 and the 4340 steel [79, 80] in Table 4.2 are taken from the literature.

### 4.1.2 Equations of State

The Mie–Grüneisen equations of state (EOS\_GRUNEISEN) are used to describe the pressure-temperature-volume thermodynamic relations in solids under shock loading [86]. This is important to include because it depicts hydrodynamic response and thermodynamic properties of material at the macroscale. The hydrostatic pressure,  $P$ , is defined as the following for compressed materials in Equation (A4.3) and for expanded materials in Equation (A4.4), respectively [70]:

$$P = \frac{\rho_0 C'^2 \mu (1 + (1 - \gamma_0/2)\mu - (a/2)\mu^2)}{[1 - (S_1 - 1)\mu - S_2 \mu^2 / (\mu + 1) - S_3 \mu^3 / (1 + \mu)^2]} + (\gamma_0 + a\mu) E' \quad (\text{A4.3})$$

$$P = \rho_0 C'^2 \mu + (\gamma_0 + a\mu) E' \quad (\text{A4.4})$$

where  $S_1$  to  $S_3$  are the slope coefficients of the shock and particle velocity curve,  $E'$  is the internal energy per unit reference specific volume,  $C'$  is the bulk speed of sound,  $\gamma_0$  is the Grüneisen gamma coefficient,  $\rho_0$  is the density at the reference state,  $a$  is the volume correction factor, and  $\mu = \rho/\rho_0 - 1$  is the volumetric strain defining current density to reference density.

Table 4.1: Material model properties and constants of the 12.7 mm armor piercing incendiary projectile.

Property/Constant	Value	Unit
Density ( $\rho$ )	7850 [2]	kg/m <sup>3</sup>
Young's Modulus ( $E$ )	200 [2]	GPa
Shear Modulus ( $G$ )	76.92 [2]	GPa
Poisson's Ratio ( $\nu$ )	0.3 [2]	-
I. Johnson-Cook Strength Model		
Static Yield Stress ( $A$ )	1.65771 [2]	GPa
Strain Hardening Constant ( $B$ )	20.8556 [2]	GPa
Strain Rate Constant ( $C$ )	0.0076 [2]	-
Strain Hardening Coefficient ( $n$ )	0.651 [2]	-
Thermal Softening Coefficient ( $m$ )	0.35 [2]	-
Working Temperature ( $T_{room}$ )	293 [2]	K
Melting Temperature ( $T_m$ )	1800 [2]	K
Specific Heat ( $c_p$ )	455 [2]	J/kg-K
Reference Strain Rate ( $\dot{\epsilon}_0$ )	1 [2]	s <sup>-1</sup>
II. Johnson-Cook Damage Model		
Damage Constant 1 ( $D_1$ )	0.0301 [2]	-
Damage Constant 2 ( $D_2$ )	0.0142 [2]	-
Damage Constant 3 ( $D_3$ )	-2.192 [2]	-
Damage Constant 4 ( $D_4$ )	0 [2]	-
Damage Constant 5 ( $D_5$ )	0.35 [2]	-
III. Mie-Grüneisen Equation of State		
Elastic Wave Velocity ( $C'$ )	4570 [86]	m/s
Slope Values 1 ( $S_1$ )	1.49 [86]	-
Slope Values 2 ( $S_2$ )	0 [86]	-
Slope Values 3 ( $S_3$ )	0 [86]	-
Grüneisen Coefficient ( $\gamma_0$ )	1.93 [86]	-
Volume Correction Factor ( $a$ )	0.5 [86]	-

Table 4.2: Material model properties and constants of the rolled homogeneous armor steel and the 4340 steel.

Property/Constant	RHA	4340 Steel	Unit
Density ( $\rho$ )	7850 [78]	7770 [79, 80]	kg/m <sup>3</sup>
Young's Modulus ( $E$ )	210 [78]	200 [79, 80]	GPa
Shear Modulus ( $G$ )	82 [78]	77 [79, 80]	GPa
Poisson's Ratio ( $\nu$ )	0.28 [78]	0.29 [79, 80]	-
I. Johnson-Cook Strength Model			
Static Yield Stress ( $A$ )	0.95 [78]	0.95 [79, 80]	GPa
Strain Hardening Constant ( $B$ )	0.56 [78]	0.725 [79, 80]	GPa
Strain Rate Constant ( $C$ )	0.014 [78]	0.015 [79, 80]	-
Strain Hardening Coefficient ( $n$ )	0.26 [78]	0.375 [79, 80]	-
Thermal Softening Coefficient ( $m$ )	1 [78]	0.625 [79, 80]	-
Working Temperature ( $T_{room}$ )	300 [42]	300 [79, 80]	K
Melting Temperature ( $T_m$ )	1793 [42]	1793 [79, 80]	K
Specific Heat ( $c_p$ )	477 [42]	477 [79, 80]	J/kg-K
Reference Strain Rate ( $\dot{\epsilon}_0$ )	1 [42]	1 [79, 80]	s <sup>-1</sup>
II. Johnson-Cook Damage Model			
Damage Constant 1 ( $D_1$ )	0.05 [42]	-0.8 [79, 80]	-
Damage Constant 2 ( $D_2$ )	3.44 [42]	2.1 [79, 80]	-
Damage Constant 3 ( $D_3$ )	-2.12 [42]	-0.5 [79, 80]	-
Damage Constant 4 ( $D_4$ )	0.002 [42]	0.002 [79, 80]	-
Damage Constant 5 ( $D_5$ )	0.61 [42]	0.61 [79, 80]	-
III. Mie-Grüneisen Equation of State			
Elastic Wave Velocity ( $C'$ )	4356 [90]	4578 [93]	m/s
Slope Values 1 ( $S_1$ )	2.18 [90]	1.33 [93]	-
Slope Values 2 ( $S_2$ )	0 [90]	0 [93]	-
Slope Values 3 ( $S_3$ )	0 [90]	0 [93]	-
Grüneisen Coefficient ( $\gamma_0$ )	1.69 [90]	1.67 [93]	-
Volume Correction Factor ( $a$ )	0 [90]	0.43 [93]	-

## 4.2 Mesh Sensitivity Analysis

The GISSMO model introduces a mesh regularization curve aimed at scaling the fracture surface of the material to provide consistent fracture predictions at different mesh sizes [69, 74]. In our impact simulations, we conducted a mesh sensitivity analysis to demonstrate that the implemented GISSMO can produce comparable fracture patterns for Armox 500T steel across different mesh sizes. Specifically, a bi-layered steel system, consisting of a 10 mm Armox 500T steel front plate and a 4.70 mm rolled homogeneous armor (RHA) steel back plate with no standoff distance, is simulated under a normal impact from a 20 mm fragment simulating projectile. The different mesh sizes (i.e., 0.2 mm, 0.35 mm, and 0.5 mm) are used to discretize the plates. Figure 6 shows the measured hole sizes of the Armox 500T steel plate after the impact at different mesh sizes. The normalized distance represents the measured position from the rear surface to the impact surface of the Armox 500T steel plate. The outcomes of our impact simulations in Figure 4.1 indicate that similar fracture patterns (i.e., hole size and plug size) of the Armox 500T steel plate at different mesh sizes are consistently simulated using the GISSMO. Consequently, according to the results in Figure ?? and Figure 4.1, the GISSMO can reduce the mesh size dependency to generate insensitive results and it is feasible to use the larger mesh size from the determined mesh regularization curve in ballistic impact simulations for Armox 500T steel.

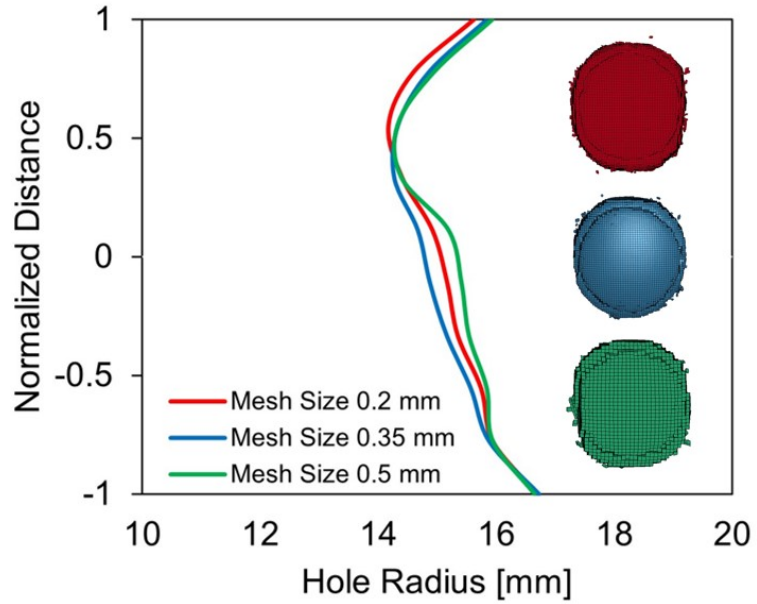


Figure 4.1: A mesh sensitivity study (i.e., mesh size 0.2 mm, 0.35 mm, and 0.5 mm) using the GISSMO in the simulations consisting of a 10 mm thick ArmoX 500T steel front plate and 4.70 mm thick rolled homogeneous armor back plate with no standoff distance under a normal impact from a 20 mm fragment simulating projectile. The simulated hole size of the ArmoX 500T steel plate and formulated plug made by the projectile are compared at different mesh sizes.